Journal of Fluids and Structures 126 (2024) 104090

Contents lists available at ScienceDirect

Journal of Fluids and Structures

journal homepage: www.elsevier.com/locate/jfs

On the coexistence of pressure regulation and oscillation modes in soft hysteretic valves

Lucas C. van Laake[1], Alberto Comoretto[1], Johannes T.B. Overvelde *

Autonomous Matter Department, AMOLF, Science Park 104, Amsterdam, 1098 XG, The Netherlands

ARTICLE INFO

Dataset link: http://dx.doi.org/10.5281/zenodo.10693369

Keywords:
Soft robotics
Fluidic circuits
Instability
Hysteretic valve

ABSTRACT

Fluidic circuits are a promising recent development in embodied control of soft robots. These circuits typically make use of highly non-linear soft components to enable complex behaviors given simple inputs, such as constant flow or pressure. This approach greatly simplifies control, as it removes the need for external hardware or software. However, detailed fundamental understanding of the non-linear, coupled fluidic and mechanical behavior of these components is lacking. Such understanding is needed to guide new designs and increase the reliability of increasingly autonomous soft robots. Here, we develop an analytical model that captures the coexistence of a pressure regulation mode and an oscillatory mode in a specific soft hysteretic valve design, that we previously used to achieve reprogrammable activation patterns in soft robots. We develop a model that describes the mechanics, fluidics and dynamics of the system by two coupled non-linear ordinary differential equations. The model shows good agreement with the experimental evidence, as well as correctly predicts the effect of design changes. Specifically, we experimentally show that we can remove the regulation mode at low input flow rates by changing the fluidic response of the valve. Taken together, the present study contributes to better understanding of system-level behavior of fluidic circuits for controlling soft robots. This may contribute to the reliability of soft robots with embodied control in future applications such as autonomous exploration and medical prosthetic devices.

1. Introduction

Soft robots are robots that consist mainly of compliant structures and materials (Ilievski et al., 2011; Rus and Tolley, 2015). This feature leads to a host of potential advantages over traditional (rigid) robotics, including intrinsic adaptability, safety, low weight, and resilience (Laschi et al., 2016). A specific challenge with soft robots in general is the design and integration of control systems. For fluid-driven soft robots in particular (Gorissen et al., 2017), which is our focus in this study, it is not straightforward to embed typical control elements such as active valves, sensors, and micro-controllers, due to the stiffness mismatch (McDonald and Ranzani, 2021). However, embedded control is a prerequisite for the development of more autonomous, untethered robotic applications (Rich et al., 2018). Therefore, there is an incentive to develop alternative control strategies that can potentially be fully soft.

For fluid-driven soft robots, a possible solution is to embed what we call fluidic circuits into their soft bodies. These fluidic circuits can be designed to behave equivalently to electronic control circuits, and can thus be used for basic control, such as actuator sequencing. Such circuits may consist of elements with linear or monotonic behavior, such as narrow tubes of specific lengths, to delay the flow of air from one actuator to the next (Vasios et al., 2020). However, a significant step towards more advanced control

* Corresponding author.
E-mail address: overvelde@amolf.nl (J.T.B. Overvelde).
[1] These two authors contributed equally.

https://doi.org/10.1016/j.jfluidstructs.2024.104090
Received 23 October 2023; Received in revised form 25 January 2024; Accepted 21 February 2024
Available online 11 March 2024

is achieved when non-linearities, and in particular instabilities and hysteresis are harnessed. For example, soft actuators may have a non-linear pressure-volume relation. This feature can be used to design sets of actuators that activate in a predetermined order when inflated or deflated (Overvelde et al., 2015; Van Raemdonck et al., 2023), or to store and release energy to make jumping robots (Gorissen et al., 2020). Gated valves, similar to transistors, expand the range of possible circuits by leveraging decades of micro-electronics motifs. This approach has been used to create state-machines (Mahon et al., 2019) and fluidic random access memory (Hoang et al., 2021), for example. All of the above designs, however, still require timed input signals to advance to the next state, or to initiate the next actuation sequence. A second significant step has led to the current state of the art, where embedded fluidic control circuits autonomously transform a constant flow or pressure input into cyclic activation of soft actuators. This was first demonstrated using an amplified microfluidics approach (Wehner et al., 2016), and has been followed by several demonstrations based on centimeter-sized non-linear valves made by casting (Rothemund et al., 2018; Van Laake et al., 2022; Park et al., 2022; Jin et al., 2023), 3D-printing techniques (Song et al., 2021; Hubbard et al., 2021; Teichmann et al., 2023; Zhai et al., 2023), or assembly (Decker et al., 2022). Their larger physical size allows the higher flow rates required to directly drive soft robotic actuators.

Among these non-linear soft robotic valves, a growing number contain domes or other snapping shells (Van Laake et al., 2022; Rothemund et al., 2018; Park et al., 2022; Jin et al., 2023). The key characteristic of such shells in this context is the hysteresis, and in some cases bistability, under pressure loading that is due to a snapping instability. This hysteresis is an essential ingredient for the generation of periodic, timed actuation of soft actuators. In previous work we used a hysteretic valve based on an elastomeric spherical cap with a slit at its pole (Van Laake et al., 2022), similar to the cap of a ketchup bottle or shower gel container (Brown, 1995). The slit functions as the valve element, as it is closed in the initial (pre-buckling) state, and open after snapping. These features enable the transformation of a constant inflow of air into timed pulses, which we used to periodically activate one or more soft bending actuators. In this relaxation oscillator circuit, the valve periodically closes and opens as a result of the dynamics of pressure build-up and release.

Outside of the scope of that work, we observe an interesting effect that we study in more detail in the current work. We observe that the valve can be in a different mode, at the same conditions where it can also oscillate. In this mode the valve remains in between the open and closed states, and maintains a nearly constant pressure drop for a wide range of flow rates. It is not well understood why this mode, that we call the regulation mode, exists and how we can control in which mode the valve will operate. On the one hand, the stability of this pressure-regulation mode is intriguing and in itself potentially useful in applications. On the other hand, its existence is troublesome when we use the hysteretic valve in applications where we rely on periodic oscillations for robot control, such as for the actuation of a soft robotic walker (Van Laake et al., 2022), or even a future soft Total Artificial Heart (Arfaee et al., 2022). Therefore, we want to understand under which conditions the pressure regulation and oscillation modes exist. And more specifically, what enables the key behavior, namely the coexistence of the two different modes at the same inflow rate.

A possible approach to this problem would be to look at the three-dimensional shell buckling problem in detail. In fact, although spherical shell snapping has been widely studied for decades, and remains an active topic to date (Reis, 2015; Champneys et al., 2019; Liu et al., 2022), the case of a spherical cap with a slit or cut at its pole under uniform pressure loading has not been treated to our knowledge. We expect that the cut acts as only a minor imperfection in the initial configuration as long as the shell is in compression. On the other hand, during or after the dynamic transition, the cut opens and this will certainly affect the mechanics, but it is not exactly known how. In the existing literature, the work that is most relevant to the mechanics of the current problem is on the effect of small imperfections or probing on shell snapping (Lee et al., 2016; Marthelot et al., 2017; Evkin and Lykhachova, 2019; Abbasi et al., 2021). Existing work that is relevant for the dynamics of the current problem includes a study on the dynamics of snapping structures, including toy 'poppers' (Pandey et al., 2014; Taffetani et al., 2018) that are geometrically similar to our valves. Interestingly, snapping has been shown to slow down near critical points due to loss of stiffness (Gomez et al., 2017). When visco-elasticity is additionally considered, the effects compound to result in extremely long snapping times (Gomez et al., 2019; Brinkmeyer et al., 2012). Yet, it remains unclear how to take into account the discrete change when the unbuckled dome suddenly loses stiffness due to loss of contact in the cut.

In this work we aim to capture the essentials of the mechanics in the simplest possible spring model, and we focus on the system–level behavior of the valve in interaction with its fluidic environment. The reason for this approach is the observation that the regulation mode is not stable without fluid flow. This suggests that we must study the mechanics and dynamics of the whole system to find the key to the system–level bistability. To do so, we develop a system–level model of the valve system with only two degrees of freedom. The model provides a mechanistic explanation for the existence of the regulation mode and thus suggests how this mode can be harnessed or suppressed. In a final step, we experimentally demonstrate our findings by creating a modified valve that cannot be in the oscillating and regulating states at the same inflow rate. This clearly demonstrates the utility of our simple model. Moreover, it is an important step towards the reliable application of hysteretic valves and fluidic circuits in real-world applications.

The remainder of the paper is organized as follows. In Section 2, the observed behavior is exemplified by three different experiments under varying load cases. In Section 3, we introduce a system–level model that describes the coupled fluidic and mechanical behavior. In Section 4, we analyze potential behaviors of this model to determine if the model describes the behavior observed in experiments. In Section 5, we extend the mechanical model by introducing a sudden weakening of the dome upon buckling, as well as a second local pressure maximum, to account for additional hysteresis. Only after introducing these features, the model reproduces the coexistence of oscillation and regulation at the same conditions. In Section 6, we experimentally demonstrate our findings by creating and testing a modified valve. We share our concluding remarks in Section 7.

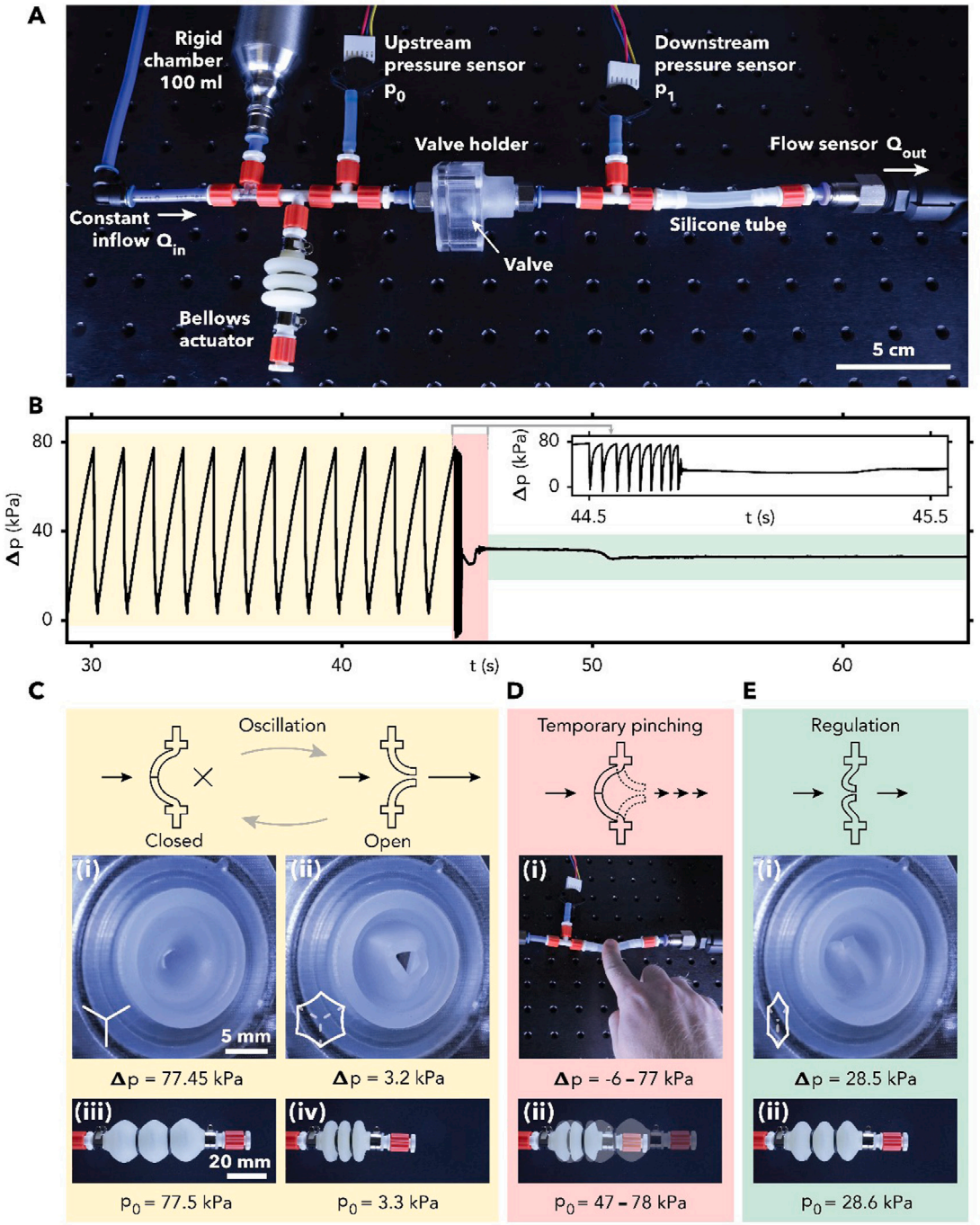

Fig. 1. A dome with a slit can be in two distinct modes at the same conditions. (A) Experimental setup with a bellows actuator and a rigid air chamber connected before a hysteretic valve, and a silicone tube directly behind the valve. (B) Pressure difference over the valve $\Delta p = p_0 - p_1$ before, during, and after temporarily pinching the silicone tube. Before pinching, the valve oscillates between its C(i) closed, and C(ii) open states, while the actuator cycles between C(iii) extended and C(iv) contracted. During D(i) pinching, the actuator temporarily D(ii) oscillates at high frequency. After pinching, the valve is in its E(i) pressure regulation mode, and the actuator is E(ii) semi-extended.

2. Experimental observations: two distinct modes at the same conditions

In order to demonstrate the potential behaviors that the dome-shaped slit-valve can exhibit, we start with a basic experiment where we place an air chamber and a soft bellows actuator before a valve, and a silicone tube behind the valve (Fig. 1A). The valve is

made by casting a dome-shaped membrane from silicone elastomer (Dragon Skin 20, Smooth-On) in a 3D printed mold (VeroClear, Stratasys). Three slits of 1.5 mm each are laser-cut at the apex, after which the valve is placed in a 3D-printed holder (Van Laake et al., 2022). We control the inflow rate Q_{in} to the air chamber using a pair of mass flow controllers (VEMD, Festo (up to 20 SLPM), in parallel with SLA5850, Brooks Instrument (up to 5 SLPM)), and measure pressures p_0 and p_1 immediately before and behind the valve, as well as flow rate Q_{out} through the valve. Throughout the first experiment, we apply a fixed inflow rate $Q_{in} = 4$ SLPM to the air chamber. This setup is similar to the fluidic relaxation oscillator that we previously studied (Van Laake et al., 2022). In order to reduce production variability, the valves in the current study are uniformly scaled up by a factor two with respect to the earlier work. Moreover, we add circular ridges inside the valve holder, to improve air-tight sealing and minimize slip of the valve's edge inside the holder. The detailed design is shown in Additional Fig. 18.

After applying the inflow, we observe that the valve is in its oscillation mode, where the pressure difference over the valve $\Delta p = p_0 - p_1$ oscillates between $\Delta p = 5$ kPa and $\Delta p = 77$ kPa (yellow shading in Fig. 1B, and Fig. 1C). We then press on the silicone tube behind the valve (red shading in Fig. 1B, and Fig. 1D), almost but not completely closing it. We observe that the valve oscillates briefly at high frequency during pinching, then stops oscillating and enters the regulation mode. After completely releasing the tube, the valve remains in this mode, and Δp stays constant at a value $\Delta p \approx 29$ kPa (green shading in Fig. 1B, and Fig. 1E), i.e., between the lowest and highest pressure observed during oscillation. Therefore, at the same experimental conditions (before and after pinching), the valve is in two different modes. In a separate experiment we place the same valve in a different holder (with the same clamping geometry) where we can observe the deformed state directly. Fig. 1C(i), C(ii), and E(i) show the valve in its three different states, and Fig. 1C(iii), C(iv), and E(ii) show the actuator in the corresponding situations.

To further describe the behavior of the valve in either mode, we perform three additional experiments. In the first additional experiment, we start from the pressure regulation mode and vary the inflow rate. Starting from an initial value of $Q_{in} = 4$ SLPM, we first increase the inflow rate to $Q_{in} = 25$ SLPM, then decrease to $Q_{in} = 0$ SLPM (Fig. 2A). We ensure the valve is in the regulation mode at the start of the experiment by briefly pinching the silicone tube. We observe that upon sweeping the inflow rate, the pressure drop over the valve remains almost constant for a wide range of inflow rates, varying between $\Delta p = 28.1$ kPa at $Q_{in} = 4$ SLPM and $\Delta p = 37.6$ kPa at $Q_{in} = 25$ SLPM (Fig. 2B), i.e., the pressure changes by 34% of the initial value. For comparison, we measured the pressure drop over a constant restriction (a needle, length 12.7 mm, internal diameter 1.54 mm). The pressure drop varies between $\Delta p = 1.85$ kPa at $Q_{in} = 4$ SLPM and $\Delta p = 50$ kPa at $Q_{in} = 25$ SLPM, i.e., 2600%, or 77 times more than the valve in regulation mode (Additional Fig. 19B). Apparently, in the regulation mode, pressure is modulated by passive adaptation of the shape of the valve, especially around the opening. At higher flow rates the opening widens, significantly lowering the effective resistance to airflow, and vice versa. Meanwhile, the overall deformation state of the membrane is in between the initial and buckled states (Fig. 2D(i)-D(iii)). When we decrease the inflow rate to $Q_{in} < 2$ SLPM, at $t \approx 80$ s, the valve exits the pressure regulation mode. As an example of an application of the pressure regulation mode, it can be leveraged to control the extension of a soft bellows actuator (Fig. 2D(v)-D(vii)).

In the second additional experiment, we start from the oscillation mode and vary the inflow rate. In response to the same flow profile shown in Fig. 2A, the oscillation frequency (Fig. 2C and E) initially increases, as the higher inflow rate causes the pressure in the air chamber to build up faster. This can be seen in Fig. 2F from the decrease in the time the valve is closed during each cycle T_{closed}. Although T_{closed} continues to decrease with inflow rate, at the same time T_{open} increases, such that from $Q_{in} > 14$ SLPM the oscillation frequency starts to decrease. Ultimately, when $Q_{in} > 20$ SLPM, oscillations stop completely, and the valve remains in the fully open state. This coincides with the inflow rate where the pressure drop over the valve in the open state is high enough to prevent the valve from buckling back. When we decrease the inflow rate, the system restarts oscillating around the same inflow rate where it stopped under increasing inflow rate. It remains in this mode until the end of the experiment.

Importantly, a clear difference in the deformed state between the fully open state and the regulation mode can be seen from comparing photographs and pressure drop over the valve at the same inflow rate $Q_{in} = 25$ SLPM in Fig. 2D. These are shown for the regulation mode in Fig. 2D(iii) (corresponding to the blue markers in Fig. 2A and B), and for the fully open state in Fig. 2D(iv) (corresponding to red markers in Fig. 2A and C).

The aim of the third additional experiment is to measure the quasi-static flow–pressure drop relation of multiple samples of the same valve design, as a basis for the development of our model, including its parameters. To measure the fully closed state and the fully open state, we connect the system to a manually controlled pressure regulator (LRP-1/4-10, Festo). This enables us to gradually vary pressure p_0, in order to accurately determine Δp_{open} and Δp_{close}. Moreover, the pressure regulator can provide higher flow rates that are beyond the range of our mass flow controller. We gradually increase the pressure p_0 before the valve until the valve opens at the pressure difference $p_0 - p_1 = \Delta p_{open}$. After the valve opens, we determine the flow–pressure drop relation in the fully open state. Finally, we decrease the pressure until the valve closes again at $p_0 - p_1 = \Delta p_{close}$. To measure the valve in its regulation mode, we connect it to a mass flow controller, and increase and decrease the flow rate, similarly to the experiment shown in Fig. 2B. We repeat these experiments for six specimens of the same valve design (Additional Fig. 19A). Finally, we record oscillations at $Q_{in} = 4$ SLPM as a reference dynamic behavior. In Fig. 3 we show the results for a representative specimen, as well as a least-squares fit to $\Delta p(Q_{out})$ in the fully open state (dashed curve). Using the fitting function $\Delta p = a\,(Q_{out})^b$ we obtain $a = (0.032 \pm 0.003)$ kPa/SLPM^b, $b = 1.68 \pm 0.04$. A constant orifice is expected to have $\Delta p \sim Q_{out}^2$ if compressibility effects are negligible (Welty et al., 2007) (compare Additional Fig. 19B).

Taken together, the experiments show that for a remarkably wide range of inflow rates 2 SLPM $< Q_{in} <$ 20 SLPM the valve can be in either the regulation mode or the oscillation mode, while for a fixed inflow rate (e.g., $Q_{in} = 4$ SLPM) the valve can be made to go from the oscillation mode to the regulation mode by briefly pressing on a flexible tube behind the valve. For a range of inflow rates 20 SLPM $< Q_{in} <$ 25 SLPM the valve can be in either the regulation mode or the fully open state.

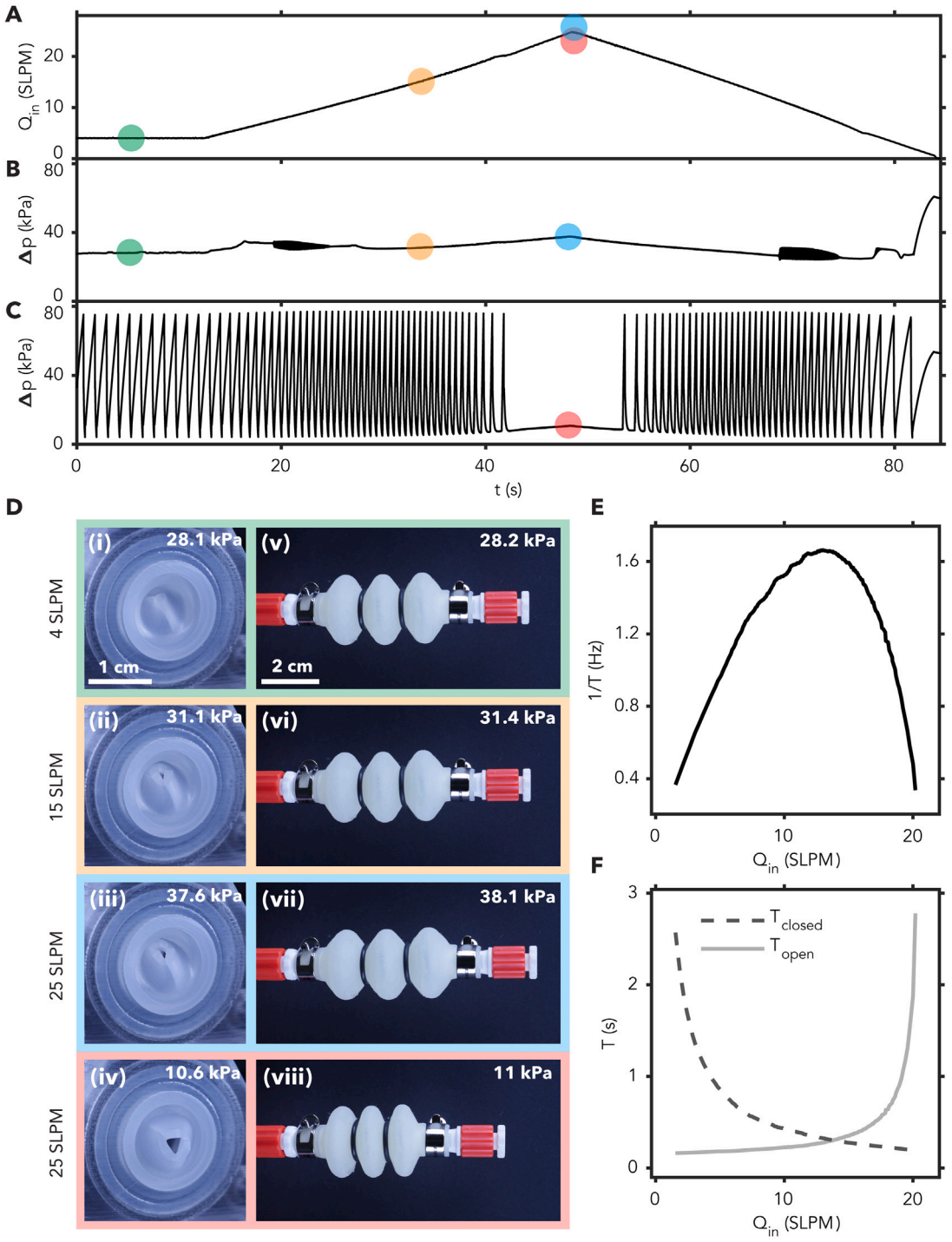

Fig. 2. Oscillating and regulation modes for varying inflow rate Q_{in}. (A) Applied inflow rate profile for both experiments. (B) and (C) Pressure difference over the valve $\Delta p = p_0 - p_1$ for (B) an experiment started from the pressure regulation mode, (C) an experiment started from the oscillation mode. (D) The valve and actuator in the regulating and fully open states. Colored borders indicate correspondence to markers of the same color in panels (A), (B) and (C). Green (i and v): regulating state at low inflow rate ($Q_{in} \approx 4$ SLPM). Orange (ii and vi): regulating state at medium inflow rate ($Q_{in} \approx 15$ SLPM). Blue (iii and vii): regulating state at high inflow rate ($Q_{in} \approx 25$ SLPM). Red (iv and viii): fully open state at high inflow rate ($Q_{in} \approx 25$ SLPM). (E) and (F) Effect of Q_{in} on (E) cycle frequency (inverse cycle time), (F) partial cycle time. Partial cycle time is the time during each cycle in which the valve is closed (dashed line) or open (solid line).

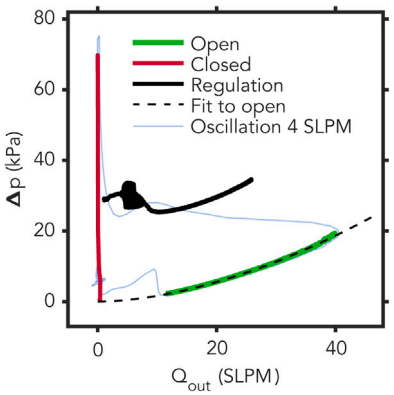

Fig. 3. Measured quasi-static pressure drop as function of outflow rate $\Delta p(Q_{\text{out}})$. Fully closed (red curve) and fully open (green curve) states are obtained in a quasi-static experiment under pressure control. Dashed line shows a fit to the open state data ($\Delta p = 0.03\,(Q_{\text{out}})^{1.68}$). The regulation mode (black curve) is obtained in a quasi-static experiment under flow control. Dynamic oscillations for $Q_{\text{in}} = 4$ SLPM (blue curve) are shown as a reference to relate the quasi-static measurements to the dynamic behavior.

3. Lumped-parameter model of the valve system

With the goal of exploring essential ingredients for coexistence of the pressure regulation and oscillation modes, we develop a minimal lumped-parameter model. We start with the description of the first order dynamics in the fluidic domain, where the valve is treated as a variable restriction. Secondly, we define a spring-model with one degree-of-freedom (DOF), to approximate the equilibrium pressure-displacement behavior of the elastomeric dome. Thirdly, we define simplified dynamics of the mechanical DOF, that describes the transitions between the open and closed states. Lastly, we explicitly define the variation of the valve orifice as a function of position of the single DOF of the mechanical spring-model. Combining these four ingredients, we obtain two coupled non-linear ordinary differential equations (ODEs) that describe the behavior of the system.

3.1. Fluidic model

The fluidic model is schematically shown in Fig. 4A(ii). A source of constant flow rate Q_{in} is connected to a pneumatic capacitor C_0 (i.e., a flexible or rigid air chamber). The valve is placed inline behind the air chamber. When the valve is open, there is an output flow Q_{out} through the valve. The pressure drop over the valve is $\Delta p = p_0 - p_1$.

We model the behavior of the capacitor linearly, where the standard volume of air V_{S} is related to pressure p_0 as

$$V_{\text{S}} = C_0 p_0, \tag{1}$$

where C_0 is the capacitance in 1/60SL/kPa (the unusual unit is a result of using the convenient units SLPM (standard litre per minute) for flow, kPa for pressure, and seconds for time).

The instantaneous variation of standard volume in the chamber is the difference between input and output flows

$$\frac{\mathrm{d}V_{\text{S}}}{\mathrm{d}t} = Q_{\text{in}} - Q_{\text{out}}, \tag{2}$$

where Q_{in} and Q_{out} are standard flows in SLPM. We assume that the pressure drop over the valve Δp is proportional to Q_{out}^2, where the square is expected for flow through a constant orifice (Welty et al., 2007), see also Additional Fig. 19B.

$$\Delta p = R_{\text{v}} Q_{\text{out}}^2, \tag{3}$$

where R_{v} is the restriction of the valve in kPa/SLPM^2, that in experiments and also in our model depends on the state of the valve (as discussed in Section 3.4). Conversely, output flow through the valve is approximately proportional to the square-root of the pressure drop

$$Q_{\text{out}} = c_{\text{v}}\sqrt{\Delta p}, \quad c_{\text{v}} = \sqrt{1/R_{\text{v}}}, \tag{4}$$

where c_{v} is the conductance of the valve in SLPM/$\sqrt{kPa}$.

From Eqs. (1), (2) and (4) we can write the dynamic equation for the fluidic system

$$C_0 \frac{\mathrm{d}p_0}{\mathrm{d}t} = Q_{\text{in}} - c_{\text{v}}\sqrt{\Delta p}. \tag{5}$$

This can be simplified further if we assume p_1 is constant

$$C_0 \frac{\mathrm{d}\Delta p}{\mathrm{d}t} = Q_{\text{in}} - c_{\text{v}}\sqrt{\Delta p}, \tag{6}$$

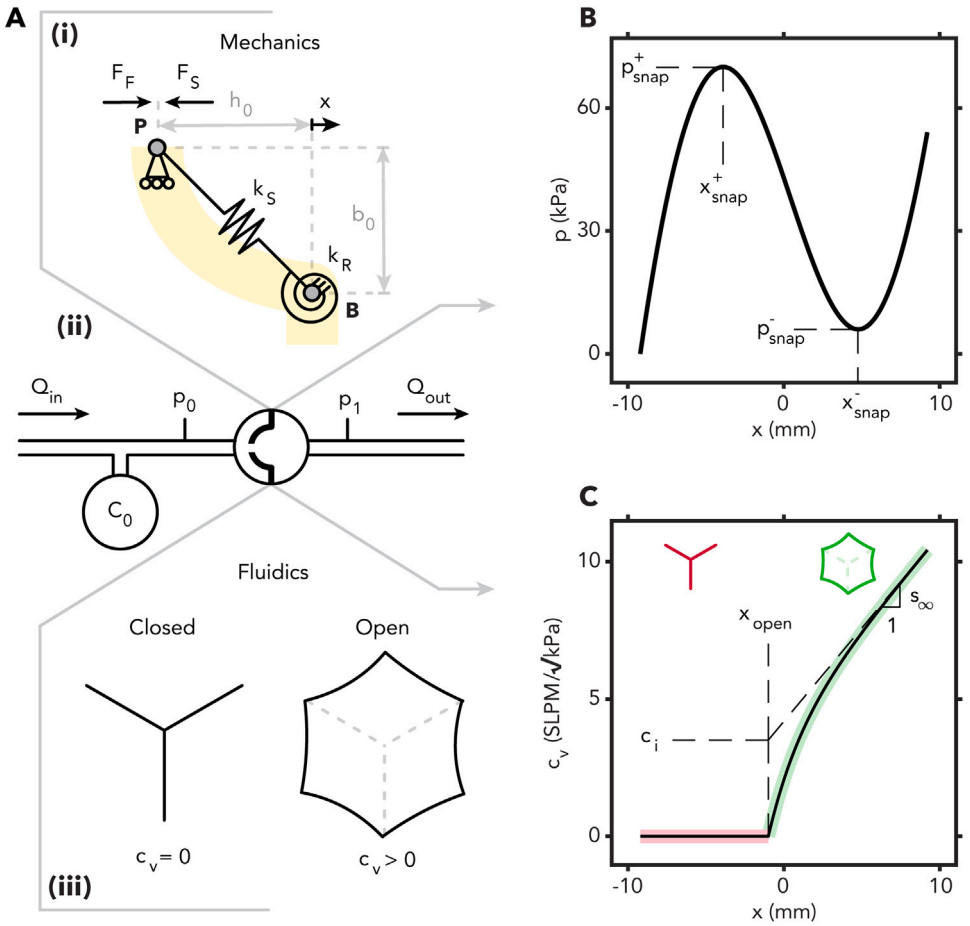

Fig. 4. Lumped-parameter model of the valve system. (A) Schematic overview of the model. (i) Mechanical spring model of the dome. (ii) Fluidic model. (iii) Valve conduction model. (B) sketch of pressure p_S, as function of displacement of node P. (C) Sketch of the conductance behavior of the valve as a function of the displacement of node P.

which is the case when the valve is venting freely to its surroundings at constant atmospheric pressure. In the general case, Eq. (5) should be used, for example when a restriction or a second air chamber, such as a soft actuator, is placed behind the valve.

The capacitance C_0 can be obtained from the slope $\mathrm{d}p_0/\mathrm{d}V_S$ in a dedicated experiment, or analytically from the geometrical volume, using the ideal gas law. For known Q_{in}, C_0 can also be conveniently determined in experiments with a hysteretic valve, from the slope $\mathrm{d}p_0/\mathrm{d}t$ when the valve is closed, i.e., $c_v = 0$, to also account for some capacitance that exists in the tubing, valve holder, and the valve itself.

3.2. Mechanics of the dome

Fig. 4A(i) shows a schematic of the model for the mechanics of the valve. A key characteristic of the mechanical response of our elastomeric dome is the existence of a local pressure maximum followed by a local pressure minimum. This behavior can be reproduced in a minimal model with only two springs. A linear spring with stiffness k_S and a rotational spring k_R account for stretching and bending, respectively.

We assume that node P is allowed to move only in the horizontal direction. Its position is equal to $x = -h_0$ at rest. Node B is constrained in both directions, therefore width b_0 is constant. An external load F_F is applied at node P in the horizontal direction. F_S is the opposing reaction force exerted by the structure. With the aim of obtaining an expression for F_S, we write the internal elastic energy E in the system, considering the geometry in Fig. 4A(i)

$$E = \frac{k_S}{2}\left(\sqrt{h_0^2 + b_0^2} - \sqrt{x^2 + b_0^2}\right)^2 + \frac{k_R}{2}\left(\arctan\left(\frac{h_0}{b_0}\right) - \arctan\left(-\frac{x}{b_0}\right)\right)^2. \tag{7}$$

The equation of the force exerted by the structure is given by the derivative of the elastic energy along the degree of freedom x

$$F_S = \frac{dE}{dx} = -k_S \frac{\sqrt{h_0^2 + b_0^2} - \sqrt{x^2 + b_0^2}}{\sqrt{x^2 + b_0^2}} x + k_R \frac{\arctan(h_0/b_0) + \arctan(x/b_0)}{b_0 (x^2/b_0^2 + 1)}. \tag{8}$$

We couple the spring model to the fluidic model by assuming the external load F_F is the net force exerted by the pressure difference over the valve, acting on the projected area of the valve A_v

$$F_F = A_v \Delta p, \quad A_v = \pi {b_0}^2, \tag{9}$$

Analogously, to transform the spring force F_S to a pressure, we divide by the valve area, such that

$$p_S = F_s / A_v. \tag{10}$$

We take b_0 to be equal to the physical radius of the valve, and h_0 the height of the dome. We then select k_s and k_r such that p_S has a local maximum $p^+_{snap}(x^+_{snap})$ and a local minimum $p^-_{snap}(x^-_{snap})$ that coincide with the experimentally observed values Δp_{open} and Δp_{close} in a slow, pressure-controlled experiment (Fig. 3). Note that the positions x^+_{snap} and x^-_{snap} also result from these assumptions and are somewhat arbitrary. This is a consequence of using a highly simplified spring model for the actual three-dimensional mechanics of the dome. In Fig. 4B we show the resulting $p_S(x)$ for $b_0 = 12\,\text{mm}, h_0 = b_0(1 - \cos\theta)/\sin\theta = 9.2\,\text{mm}, k_S = 2.9 \times 10^7\,\text{N mm}^{-1}$, and $k_R = 3.6 \times 10^8\,\text{N mm rad}^{-1}$. Notice how the negative slope in the force–displacement behavior leads to an instability if the loading is pressure–controlled. This instability gives rise to the desired hysteresis of the valve. The left and right sections with positive slope represent the valve in the initial and buckled states, respectively.

3.3. Simplified dynamics of the spring model

We define the transitions between open and closed states of the valve by simplified dynamics of x. We first write the force balance for a concentrated mass m located at P

$$F_F = m \frac{d^2x}{dt^2} + b \frac{dx}{dt} + F_S, \tag{11}$$

where b is a damping coefficient. To minimize the number of DOFs, we ignore inertial effects, based on the observation that the transitions occur relatively fast in experiments, so we obtain

$$\frac{dx}{dt} = \frac{1}{b}(F_F - F_S) = \frac{A_v}{b}(\Delta p - p_S). \tag{12}$$

We study the effect of parameter b in Section 4.3, where we analyze the stability of the system.

3.4. Valve conductance as function of node position

The second coupling between the spring model and the fluidic model is *via* the valve conductance. The exact evolution of valve conductance (see Eq. (4) for its definition) during the opening and closing of the valve is not easily observable. However, we know that the conductance must vary significantly with x to enable the regulation mode, since the pressure drop over the valve varies little for a wide range of flow rates, while the overall deformation state (associated with x) also does not change much. Moreover, we observe that the valve remains hermetically closed ($c_v = 0$) at least until the valve buckles. We define a position x_{open} where the valve starts to open ($c_v > 0$ for $x > x_{open}$). Finally, the experimental data shows that the pressure drop in the fully open state is approximately proportional to the outflow rate to the power 1.68, as shown in Fig. 3. This exponent, less than 2, implies that the orifice size continues to grow moderately with increasing position in the fully open state, according to our assumed quadratic relation between pressure and flow rate Eq. (3). This is consistent with visual observation of the orifice. We can reproduce these features by the following definition of conductance c_v as function of position x.

$$c_v = \begin{cases} 0 & x \le x_{open} \\ c_i \left(1 - e^{\psi(x_{open} - x)}\right) + s_\infty (x - x_{open}) & x > x_{open}, \end{cases} \tag{13}$$

where ψ sets the rate at which c_v approaches the value c_i and s_∞ is the remaining slope for $x \gg x_{open}$, as shown in Fig. 4C. For different values of x_{open} and ψ, we can determine c_i, and s_∞ by fitting the model to measured values $\Delta p(Q_{in})$. We study the effect of these parameters in Section 4.2.

3.5. System model

Combining the fluidic model, the spring model, and the conductance behavior, we obtain the following set of two ordinary differential equations in Δp and x.

$$\frac{d\Delta p}{dt} = \frac{1}{C_0}\left(Q_{in} - c_v(x)\sqrt{\Delta p}\right), \tag{14}$$

$$\frac{dx}{dt} = \frac{A_v}{b}\left(\Delta p - p_S(x)\right), \tag{15}$$

where $c_v(x)$ is defined in Eq. (13) (Fig. 4C), and $p_S(x)$ in Eqs. (8) and (10) (Fig. 4B). Note that all parameters are positive.

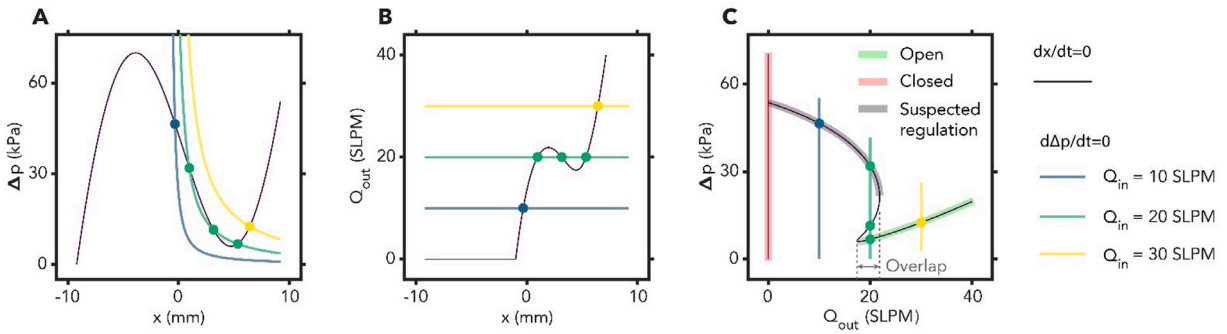

Fig. 5. Three projections of the nullclines of the initial model. (A-C) Nullclines $\mathrm{d}x/\mathrm{d}t = 0$ (black) and $\mathrm{d}\Delta p/\mathrm{d}t = 0$ (colored) in the (A) x–Δp plane, (B) x–Q_{out} plane, and (C) Q_{out}–Δp plane. Highlights in panel (C) correspond to features of the model that are similar to the experimentally observed behavior as shown in Fig. 3.

4. Potential behaviors of the initial model

Having established an initial and highly simplified model, we want to determine if the model can describe the observed behavior in the specific configurations for which we presented the experimental data in Figs. 1, 2 and 4. Therefore, rather than studying the model behavior for a wide range of parameter values, we fix as many parameters as possible based on the available experimental data. This is possible for the parameters of the spring model b_0, h_0, k_{S}, and k_{R}, as well as the parameters that we control in experiments Q_{in} and C_0. On the other hand, we cannot directly obtain all fluidics parameters x_{open}, ψ, c_{i}, s_∞, nor the damping parameter b from measurements. Therefore, we perform parameter scans for these parameters in order to find values that are compatible with the observed behavior.

The observed behavior we are trying to describe consists of the coexistence of regulation and oscillation for $2\,\mathrm{SLPM} < Q_{\mathrm{in}} < 20\,\mathrm{SLPM}$, and coexistence of regulation and the fully open state for $20\,\mathrm{SLPM} < Q_{\mathrm{in}} < 25\,\mathrm{SLPM}$. The pressure drop over the valve in the regulation mode varies from $\Delta p \approx 25\,\mathrm{kPa}$ at relatively low flow, to $\Delta p \approx 40\,\mathrm{kPa}$ at relatively high flow. Importantly, the regulation mode is stable for a wide range of flow rates, based on two observations. (1) The valve is attracted to the regulation mode when we temporarily perturb the system (Fig. 1). This leads to the conclusion that the regulation mode is a stable equilibrium. (2) The valve remains in the regulation mode when we vary the inflow rate (Fig. 2). This shows that the equilibrium remains stable at different inflow rates.

Therefore, to explain the regulation mode, we need to find equilibria at a range of pressure values around $\Delta p \approx 30\,\mathrm{kPa}$, that are stable for a range of inflow rates around $2\,\mathrm{SLPM} < Q_{\mathrm{in}} < 25\,\mathrm{SLPM}$, similar to the black curve in Fig. 3. At the same time, there must exist stable limit cycles, at the same flow rates, that describe the oscillation mode, similar to the blue curve in Fig. 3. To determine if parameters exist for which the current model can describe both behaviors, we firstly analyze the general existence of equilibria, using arbitrary parameter values for the fluidics, in Section 4.1. In Section 4.2, we investigate the influence of fluidics parameters (x_{open} and ψ) on the shape of these equilibria. In Section 4.3 we analyze the effect of damping parameter b on the stability of the existing equilibria. Finally, we look at the relation between the existence of stable equilibria (regulation mode) and limit cycles (oscillation mode).

4.1. System equilibria

To determine all possible equilibria, we begin by looking at the nullclines for Δp and x, respectively,

$$\frac{\mathrm{d}\Delta p}{\mathrm{d}t} = 0 \iff Q_{\mathrm{in}} = c_{\mathrm{v}}(x_{\mathrm{eq}})\sqrt{\Delta p_{\mathrm{eq}}}, \tag{16}$$

$$\frac{\mathrm{d}x}{\mathrm{d}t} = 0 \iff \Delta p_{\mathrm{eq}} = p_{\mathrm{S}}(x_{\mathrm{eq}}). \tag{17}$$

When the valve is closed ($x \le x_{\mathrm{open}}$, $c_{\mathrm{v}} = 0$) we find from Eq. (16) that the system is in equilibrium only for $Q_{\mathrm{in}} = 0$. In that situation, the coupling between Δp and x reduces to the mechanical model Eq. (15), and the equilibria follow from Eq. (17)

$$\Delta p(x_{\mathrm{eq}}) = p_{\mathrm{S}}(x_{\mathrm{eq}}). \tag{18}$$

When the valve is open ($x > x_{\mathrm{open}}$), we can substitute Eq. (17) in Eq. (16) to find the equilibria $(x_{\mathrm{eq}}, \Delta p_{\mathrm{eq}})$. At equilibrium, the outflow rate must equal the inflow rate. All equilibria are therefore described by the single equation

$$Q_{\mathrm{in}} = Q_{\mathrm{out}} = c_{\mathrm{v}}(x_{\mathrm{eq}})\sqrt{p_{\mathrm{S}}(x_{\mathrm{eq}})}. \tag{19}$$

This observation allows us to project Eqs. (16) and (17) on any of the three two-dimensional projections of the system x–Δp–Q_{out}. We illustrate these projections in Fig. 5, using representative values for the mechanics, but arbitrary parameter values for the fluidics. In

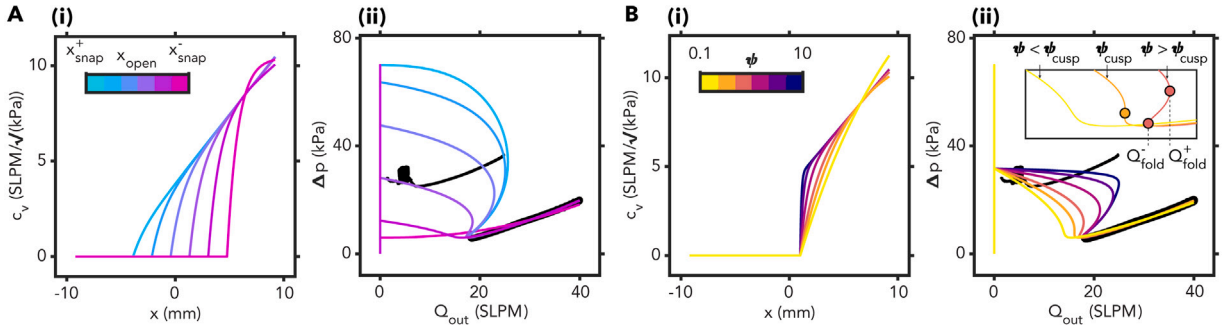

Fig. 6. Effect of valve conduction parameters on system equilibria. (A) Effect of x_{open} for a constant value of $\psi = 1\,\mathrm{mm}^{-1}$. (B) Effect of ψ for a constant value of $x_{open} = 1\,\mathrm{mm}$. The left column (i) shows the relation $c_v(x_{eq})$. The right column (ii) shows the resulting nullcline $\mathrm{d}x/\mathrm{d}t = 0$ (colored lines). Solid black lines show the experimentally obtained reference curves for the regulation mode and fully open state.

Fig. 5A we show the solutions to Eqs. (16) and (17) in the x–Δp plane for $Q_{in} = 10$, 20, and 30 SLPM. In this projection, the nullcline $\mathrm{d}x/\mathrm{d}t = 0$ (black line) is equivalent to the behavior of $p_S(x)$ (Fig. 4B). The nullclines $\mathrm{d}\Delta p/\mathrm{d}t = 0$ (colored lines) are determined by rewriting Eq. (19) as follows

$$\Delta p_{eq} = \left(Q_{in}/c_v(x_{eq})\right)^2. \tag{20}$$

The points where two nullclines cross indicate the points where the fluidic and mechanical pressure/force equilibrate. As such, higher flow rates lead to higher values of x. Moreover, for some flow rates (e.g., for $Q_{in} = 20$ SLPM)) we observe multiple equilibrium points. In Fig. 5B, we show the same nullclines in the x–Q_{out} plane. The nullclines $\mathrm{d}\Delta p/\mathrm{d}t = 0$ (colored lines) are conveniently transformed to straight lines, since $Q_{in} = Q_{out}$. This makes it straightforward to find the equilibria for any inflow rate Q_{in} from inspecting only the single nullcline $\mathrm{d}x/\mathrm{d}t = 0$. The nullcline $\mathrm{d}x/\mathrm{d}t = 0$ (black line) is described by Eq. (19). In Fig. 5C, we show the mapping of the unique values $Q_{out}(x_{eq})$ and $\Delta p(x_{eq})$ onto the Q_{out}–Δp plane. This final mapping is most convenient for our purposes, since Δp and Q_{out} are the variables that we measure in experiments, such that this projection enables a direct comparison with experimental data.

Comparing the nullclines shown in Fig. 5C to the experimentally observed behavior Fig. 3, we see four similarities.

1. The closed state of the valve is described by a vertical section at $Q_{in} = 0$.
2. The fully open state of the valve is represented by a section starting at the local pressure minimum around $Q_{in} \approx 18$ SLPM, $\Delta p \approx 5$ kPa, and extending (infinitely) to higher flows and pressures.
3. There is a section connecting the previous two, that spans approximately the same pressure and flow ranges as the experimentally observed regulation mode. (In the following points we refer to this section as the suspected regulation mode.)
4. The range of inflow rates for which the suspected regulation mode exists, partially overlaps with the range of inflow rates for which the fully open state exists.

A qualitative difference is that in the model the suspected regulation mode has a negative slope, while in the experimental data the regulation mode has a positive slope.

4.2. Equilibria as function of conduction parameters

We have determined the general existence of equilibria and identified a part of the nullcline $\mathrm{d}x/\mathrm{d}t = 0$ that potentially describes the regulation mode. In the current section we study how the equilibria change when we vary model parameters. The nullclines of our initial model depend only on the spring model and conductance behavior. The assumptions presented in Section 3.2 fully constrain the parameters of the spring model based on experimental data. We therefore turn our attention to the conductance behavior, i.e., the fluidics parameters x_{open}, ψ, c_i and s_∞.

We seek to optimize the fit between model and experimental values for $\Delta p(Q_{out})$ in the regulation mode, under the constraint that $\Delta p(Q_{out})$ in the fully open state is also matched. We select x_{open} and ψ as the free parameters. For different combinations of x_{open} and ψ we perform a two-parameter fit to open state data to obtain c_i and s_∞. In Fig. 6 we show the resulting conductance behaviors and nullclines alongside the measured data. Increasing x_{open} (Fig. 6A(i)) leads to a decrease of the pressure at low flow (Fig. 6A(ii)). The pressure at $Q_{out} = 0$ is equal to $p_S(x_{open})$. Experimentally, the regulation mode occurs at pressure differences around $\Delta p \approx 30$ kPa. This is best approximated for $x_{open} \approx 1$ mm.

Increasing ψ (Fig. 6B(i)) flattens $\Delta p(Q_{out})$, but the slope remains negative. The experimental behavior has a slightly positive slope. Therefore, the fit to the measured data continues to improve as $\psi \to \infty$. As a result, we do not find an upper bound on ψ from this analysis. Conversely, decreasing ψ decreases the range of flow rates for which regulation and oscillation could coexist, i.e., Q^+_{fold} decreases. Below a critical value $\psi = \psi_{cusp} \approx 0.22\,\mathrm{mm}^{-1}$, the regulation mode and the fully open state cannot coexist altogether. Since this contradicts the experimental observations, we will use $\psi > \psi_{cusp}$ as a lower bound in our further analysis.

The result of this section is that we have narrowed the feasible range for four model parameters. We get the best fit with experimental data for $x_{\text{open}} \approx 1\,\text{mm}$ and $\psi > \psi_{\text{cusp}} \approx 0.22\,\text{mm}^{-1}$. For different values of ψ, we find c_i and s_∞ by fitting to experimental data. We show the resulting values for c_i and s_∞ in Additional Fig. 23.

The nullclines for $x_{\text{open}} = 1\,\text{mm}$ and $\psi > 0.22\,\text{mm}^{-1}$ show that there exist equilibria at pressure and inflow values similar to those we observed experimentally in the regulation mode, albeit with negative slope instead of the positive slope that we observe in experiments. This suggests that the model could potentially reproduce the observed behavior, but only if these equilibria are stable in the regulation mode, and only if there also exists an oscillation mode at the same inflow rates. To determine if this can be the case, we need to study the dynamics of the system, i.e., the stability of the equilibria as well as the possible (co-)existence of stable points and limit cycles.

4.3. Stability of the equilibria

Thus far, we have determined approximate values for all parameters except for ψ and b. In this section, we study if there is any combination of values for ψ and b that leads to stability of the regulation mode as well as the existence of the oscillation mode. This will finalize our analysis of the initial model, and allows us to determine if the model is capable of capturing the qualitative behavior observed in experiments.

We begin by assessing the stability of the equilibria. For the valve in the closed state ($x \le x_{\text{open}}$), the system reduces to Eq. (15), and stability can be determined from

$$\partial\left(\frac{\mathrm{d}x}{\mathrm{d}t}\right)/\partial x < 0 \iff = -\frac{A_\text{v}}{b}\frac{\partial p_\text{S}}{\partial x} < 0 \iff \frac{\partial p_\text{S}}{\partial x} > 0, \quad x \le x_{\text{open}}. \tag{21}$$

For $x > x_{\text{open}}$, we write the Jacobian matrix of the system

$$J = \begin{bmatrix} \partial\left(\frac{\mathrm{d}\Delta p}{\mathrm{d}t}\right)/\partial \Delta p & \partial\left(\frac{\mathrm{d}\Delta p}{\mathrm{d}t}\right)/\partial x \\ \partial\left(\frac{\mathrm{d}x}{\mathrm{d}t}\right)/\partial \Delta p & \partial\left(\frac{\mathrm{d}x}{\mathrm{d}t}\right)/\partial x \end{bmatrix}\Bigg|_{x_\text{eq}} = \begin{bmatrix} -\frac{c_\text{v}(x)}{2C_0}\frac{1}{\sqrt{p_\text{S}(x)}} & -\frac{\sqrt{p_\text{S}(x)}}{C_0}\frac{\partial c_\text{v}}{\partial x} \\ \frac{A_\text{v}}{b} & -\frac{A_\text{v}}{b}\frac{\partial p_\text{S}}{\partial x} \end{bmatrix}\Bigg|_{x_\text{eq}}, \tag{22}$$

where

$$\frac{\partial c_\text{v}}{\partial x} = \psi\, c_\text{i}\, e^{\psi\,(x_{\text{open}} - x)} + s_\infty, \tag{23}$$

and

$$\frac{\partial p_\text{S}}{\partial x} = \frac{1}{A_\text{v}}\left(\frac{k_\text{r}}{{b_0}^2\left(\frac{x^2}{{b_0}^2}+1\right)^2} - \frac{k_\text{s}\left(\sqrt{{b_0}^2+{h_0}^2} - \sqrt{{b_0}^2+x^2}\right)}{\sqrt{{b_0}^2+x^2}} + \frac{k_\text{s}\,x^2}{{b_0}^2+x^2} + \frac{k_\text{s}\,x^2\left(\sqrt{{b_0}^2+{h_0}^2} - \sqrt{{b_0}^2+x^2}\right)}{\left({b_0}^2+x^2\right)^{3/2}} - \frac{2\,k_\text{r}\,x\left(\operatorname{atan}\left(\frac{h_0}{b_0}\right) + \operatorname{atan}\left(\frac{x}{b_0}\right)\right)}{{b_0}^3\left(\frac{x^2}{{b_0}^2}+1\right)^2}\right). \tag{24}$$

Note that the inflow rate does not appear in the Jacobian. That is because for any equilibrium position the associated inflow rate $Q_\text{in}(x_\text{eq})$ can be inferred, according to Eq. (19).

If both eigenvalues λ_1 and λ_2 of the Jacobian, evaluated at an equilibrium position x_eq, are negative, the equilibrium is stable. For a two-DOF system, this can be determined following

$$\lambda_\text{i} < 0 \quad (i = 1, 2) \quad \iff \quad \det(J) = \lambda_1\,\lambda_2 > 0 \quad \wedge \quad \operatorname{tr}(J) = \lambda_1 + \lambda_2 < 0. \tag{25}$$

Considering the first condition needed for stability, we write the determinant of the Jacobian

$$\det(J) = \frac{A_\text{v}\left(c_\text{v}(x)\frac{\partial p_\text{S}}{\partial x} + 2\,p_\text{S}(x)\frac{\partial c_\text{v}}{\partial x}\right)}{2\,b\,C_0\sqrt{p_\text{S}(x)}}\Bigg|_{x_\text{eq}} > 0. \tag{26}$$

Since the isolated spring model, without fluidic effects, is monostable,

$$p_\text{S}(x) > 0 \quad \forall \quad x > -h_0, \tag{27}$$

Eq. (26) holds if

$$c_\text{v}(x)\frac{\partial p_\text{S}}{\partial x} + 2\,p_\text{S}(x)\frac{\partial c_\text{v}}{\partial x} > 0. \tag{28}$$

As p_S, $c_\text{v}(x)$, and its derivative $\partial c_\text{v}/\partial x$ are greater than zero for $x > x_{\text{open}}$, the determinant is positive for positions where the pressure–displacement curve has positive slope, i.e., where the spring model has positive differential stiffness

$$\frac{\partial p_\text{S}}{\partial x} > 0 \Rightarrow \det(J) > 0. \tag{29}$$

Table 1
Parameters used for the stability analysis of the initial model.

Parameter	Value	Unit
b_0	12	mm
h_0	9.2	mm
θ	75	deg
A_v	452.4	mm^2
k_S	2.9×10^7	$N\,mm^{-1}$
k_R	3.6×10^8	$N\,mm\,rad^{-1}$
C_0	0.06	1/60SL/kPa
x_{open}	1	mm
ψ	10	mm^{-1}
c_i	4.5	$SLPM/\sqrt{kPa}$
s_∞	0.7	$SLPM/\sqrt{kPa}/mm$

In the negative differential stiffness region, the Jacobian only has a positive determinant if

$$\frac{\psi\, e^{\psi(x_{open}-x)} + s_\infty/c_i}{1 - e^{\psi(x_{open}-x)} + s_\infty/c_i\,(x - x_{open})} > -\frac{1}{2\,p_S(x)}\frac{\partial p_S}{\partial x}, \quad x > x_{open}, \tag{30}$$

where we use Eq. (23) to highlight the dependence on ψ.

Note that Eq. (28) implies positive slope $\partial Q_{out}/\partial x$, since

$$\begin{aligned} Q_{out,eq} &= c_v(x)\sqrt{p_S}, \\ \frac{\partial Q_{out}}{\partial x} &= \frac{\partial c_v}{\partial x}\sqrt{p_S} + c_v(x)\frac{1}{2\sqrt{p_S}}\frac{\partial p_S}{\partial x}, \\ \frac{\partial Q_{out}}{\partial x} > 0 &\iff c_v(x)\frac{\partial p_S}{\partial x} + 2\,p_S(x)\frac{\partial c_v}{\partial x} > 0 \Rightarrow \det(J) > 0, \end{aligned} \tag{31}$$

which further implies negative slope $\partial p_S/\partial Q_{out}$ in the negative differential stiffness region of the mechanics ($\frac{\partial p_S}{\partial x} < 0$), since

$$\begin{aligned} \frac{\partial Q_{out}}{\partial x} &= \frac{\partial p_S}{\partial x}\Big/\frac{\partial p_S}{\partial Q_{out}}, \\ \frac{\partial Q_{out}}{\partial x} > 0 &\iff \operatorname{sign}\left(\frac{\partial p_S}{\partial x}\right) = \operatorname{sign}\left(\frac{\partial p_S}{\partial Q_{out}}\right). \end{aligned} \tag{32}$$

This means that those equilibria for which $\partial p_S/\partial Q_{out} > 0$ and $\partial p_S/\partial x < 0$ are unstable (saddle points, $\det(J) < 0$) for any value of damping parameter b.

For the second condition for stability, we require that the trace of the Jacobian is negative

$$\operatorname{tr}(J) = -\frac{c_v(x)}{2\,C_0}\frac{1}{\sqrt{p_S(x)}} - \frac{A_v}{b}\left.\frac{\partial p_S}{\partial x}\right|_{x_{eq}} < 0. \tag{33}$$

The first term of Eq. (33) is always less than or equal to zero. Therefore, the trace is always negative when the spring model has positive differential stiffness

$$\frac{\partial p_S}{\partial x} > 0 \Rightarrow \operatorname{tr}(J) < 0 \tag{34}$$

For the region of the spring model behavior that has negative differential stiffness, the trace of the Jacobian is only negative for a minimum value of damping, as we see from rearranging Eq. (33)

$$b > -\left(\frac{2\,A_V\,C_0}{c_v(x)}\right)\frac{\partial p_S}{\partial x}\sqrt{p_S(x)}, \quad x > x_{open}. \tag{35}$$

From Eqs. (21), (25), (29) and (34) we find that equilibrium positions where the spring model has positive differential stiffness are always stable. For the region with negative slope, Eqs. (30) and (35) allow us to determine parameter values ψ and b for which the regulation mode is stabilized. We can see that these values will be different for varying equilibrium positions x_{eq}. Since we also know the unique equilibrium inflow rate associated with any equilibrium position $Q_{in}(x_{eq})$ according to Eq. (19), we can determine a range of inflow rates for which the regulation mode is stable, as function of ψ and b.

In Fig. 7 we show the flow rates for which the regulation mode is stable, for $\psi = \psi_{cusp}$, 1, 10, and $100\,mm^{-1}$, and damping value $1 \le b \le 1 \times 10^6\,N\,s\,mm^{-1}$. The minimum flow rate (orange curve) follows from Eq. (35) ($\operatorname{tr}(J) < 0$). The maximum flow rate (blue lines and blue projected curve) follows from Eq. (30) ($\det(J) > 0$). As an example, we highlight the stable region in the plane defined by $\psi = 10\,mm^{-1}$ (green area in Fig. 7). To illustrate the effect of b, we study the system response in more detail for four points marked b_1, b_2, b_3, b_4 on the line defined by $\psi = 10\,mm^{-1}$ and $Q_{in} = 15\,SLPM$. For these values of ψ and Q_{in}, the minimum damping to achieve stability is $b = 1230\,N\,s\,mm^{-1}$. The first two points ($b_1 = 1$ and $b_2 = 100\,N\,s\,mm^{-1}$) are in the unstable regime. The other two points ($b_3 = 1 \times 10^4$ and $b_4 = 1 \times 10^6\,N\,s\,mm^{-1}$), are in the stable regime.

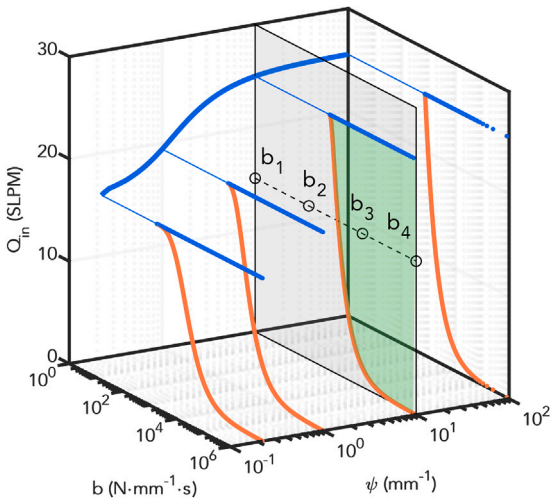

Fig. 7. Stability of the suspected regulation mode. Areas between blue lines and orange curves are stable. As an example, the stable region for $\psi = 10\,\mathrm{mm}^{-1}$ is colored green. The dynamic response of markers b_1, b_2, b_3, and b_4 is exemplified in Fig. 8. The used parameter values are listed in Table 1.

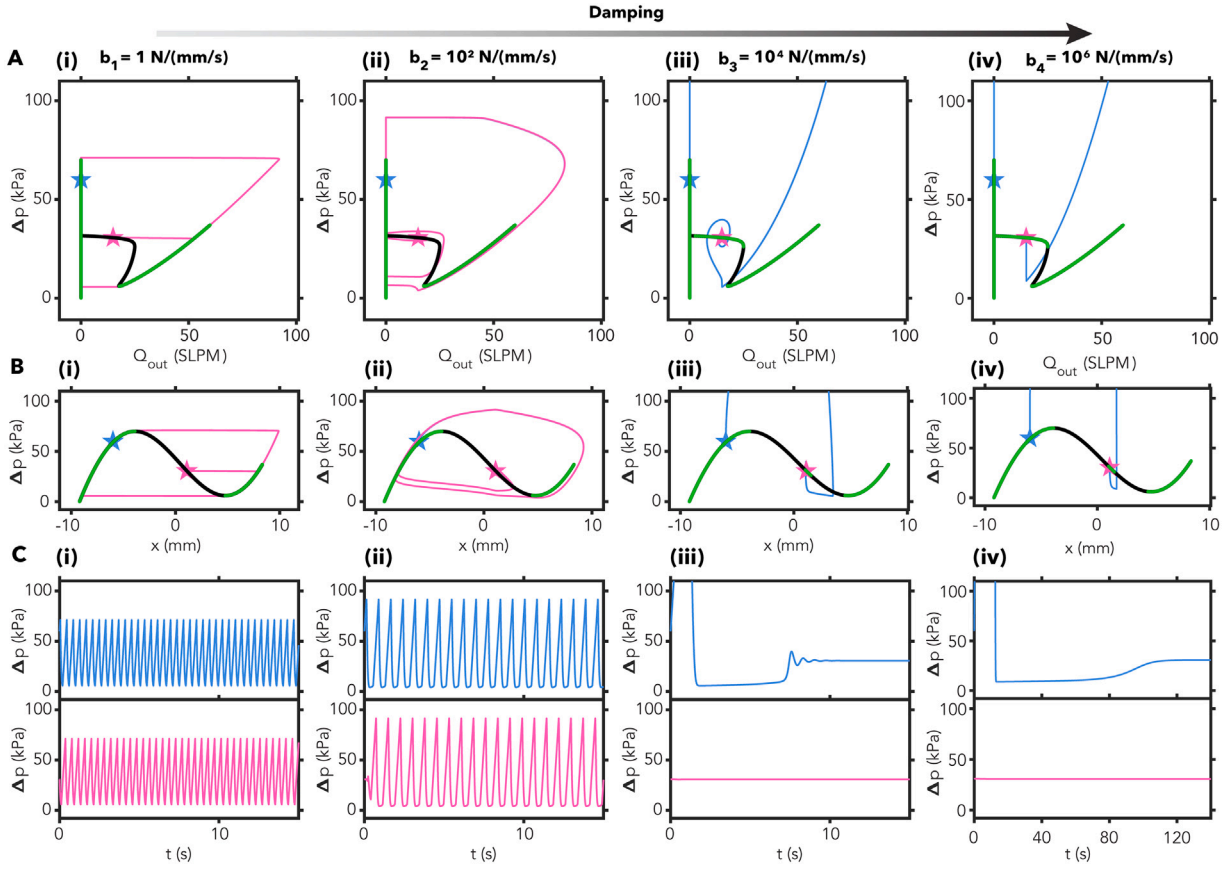

Fig. 8. Simulated effect of damping parameter b on the dynamic response of the initial model. (A) and (B) Simulated trajectories (blue and magenta curves) for two different initial conditions (blue and magenta stars), both for $Q_{in} = 15\,\mathrm{SLPM}$, are shown in the Q_{out}–Δp plane (A), and in the x–Δp plane (B). Black curves represent The nullcline $\mathrm{d}x/\mathrm{d}t = 0$, where green overlay corresponds to stable equilibria. (C) Simulated pressure difference Δp over the valve for the same trajectories shown in (A) and (B). Columns (i) to (iv) show results for increasing values of b, as indicated. Parameter values are listed in Table 1.

In Fig. 8 we show the system response for different values of damping parameter b (corresponding to markers b_1 to b_4 in Fig. 7). The other parameter values are summarized in Table 1. Although we use $\psi = 10\,\mathrm{mm}^{-1}$, similar transitions are observed for higher or

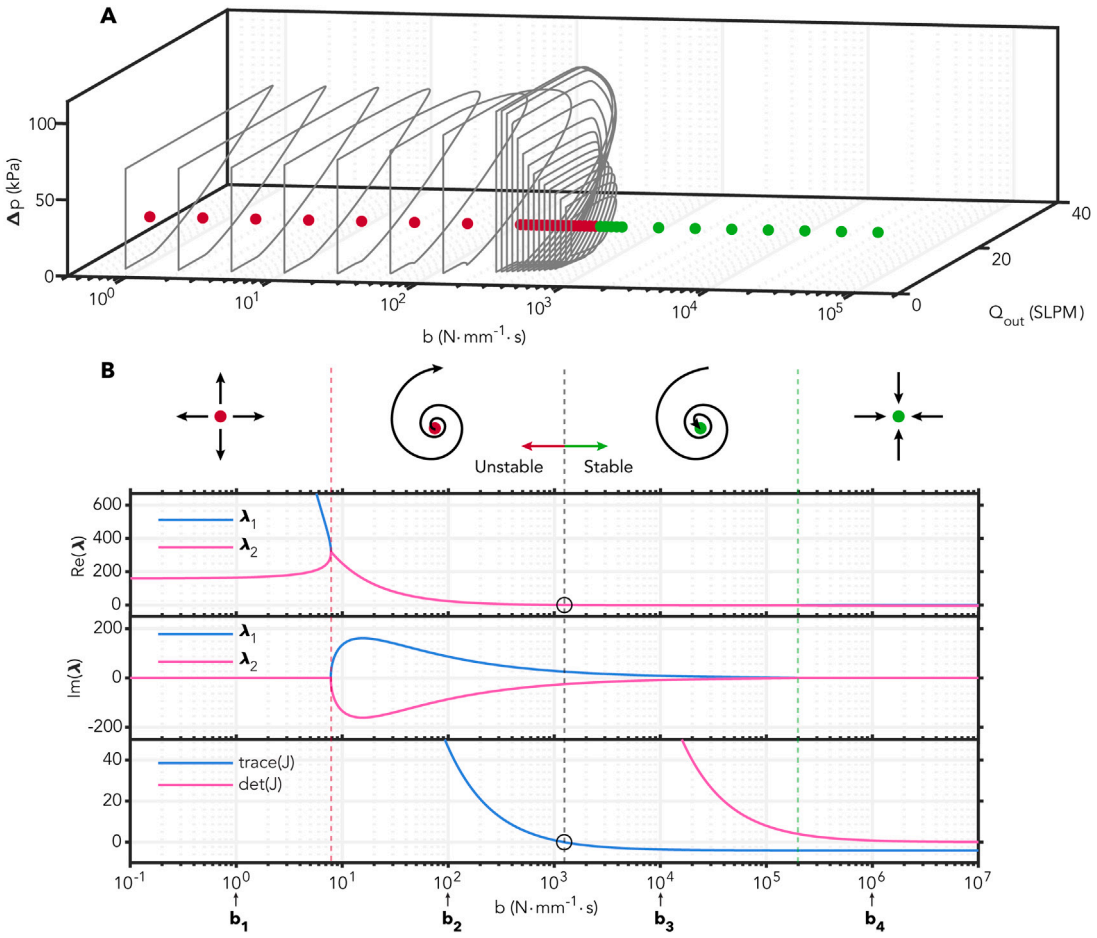

Fig. 9. Simulated effect of damping on stability of oscillation and suspected regulation modes in the initial model, for Q_{in} = 15 SLPM. (A) Stable limit cycles (gray curves) in the Q_{out}–Δp plane for different values of damping b. The single equilibrium changes from unstable (red) to stable (green). (B) Real and imaginary parts of the eigenvalues of the Jacobian and trace and determinant of the Jacobian. Flow symbols indicate (from left to right) unstable node, unstable spiral, stable spiral, stable node. Open circular marker indicates transition to stability. Parameter values are listed in Table 1.

lower values of ψ and other values of inflow rate $0 < Q_{in} < Q^{-}_{fold}$ (see Fig. 6 for the definition of Q^{-}_{fold}). In Fig. 8A and B we show the nullclines in the Q_{out}–Δp plane and x–p plane, respectively. We evaluate the stability and color the stable parts of the nullcline green. Note that green coloring means these points are stable if and only if the associated inflow rate $Q_{in,eq} = Q_{out,eq}$ is applied. We also show two trajectories, one starting close to the expected limit cycle for oscillation (blue star and curve), and another starting close to the regulation mode (magenta star and curve), both for Q_{in} = 15 SLPM. Additionally, we show these trajectories as a function of time in Fig. 8C.

As expected from Fig. 7, at low damping (Fig. 8A-C (i) and (ii)) there are no flow rates for which the regulation mode is stable. Only the fully open and closed states are colored green. For higher values of b, the suspected regulation mode is stable for a wide range of inflow rates (iii) and (iv). Note that the applied flow rate Q_{in} = 15 SLPM lies within this range and the equilibrium is therefore stable.

These results show that the suspected regulation mode can be stabilized by sufficiently high damping. However, increased damping also strongly affects the oscillation mode. At low damping (Fig. 8A-C (i)) we see relaxation oscillations with maximum pressure close to Δp_{open}, i.e., close to the value at which the valve opens in a quasi-static experiment (Fig. 3). This agrees with the observed behavior in experiments (Figs. 2 and 3). Higher damping slows down the transitions between open and closed states, which increases Δp_{max} and decreases the cycle frequency (Fig. 8A-C (ii)). More importantly, at the same step in damping value for which the suspected regulation mode appears, the oscillation mode disappears altogether (Fig. 8A-C (iii) and (iv)). Therefore, in this analysis, we do not find any combination of parameters in line with experimental observations, for which the current model explains the coexistence of the regulation and oscillation modes.

Note that the step in damping value from b_2 to b_3 is still two orders of magnitude. To better understand this transition and to ensure that coexistence does not exist at intermediate values, we perform a numerical bifurcation analysis. We determine the eigenvalues of the Jacobian for the equilibrium at Q_{in} = 15 SLPM as a function of b, and we find the limit cycle of the system

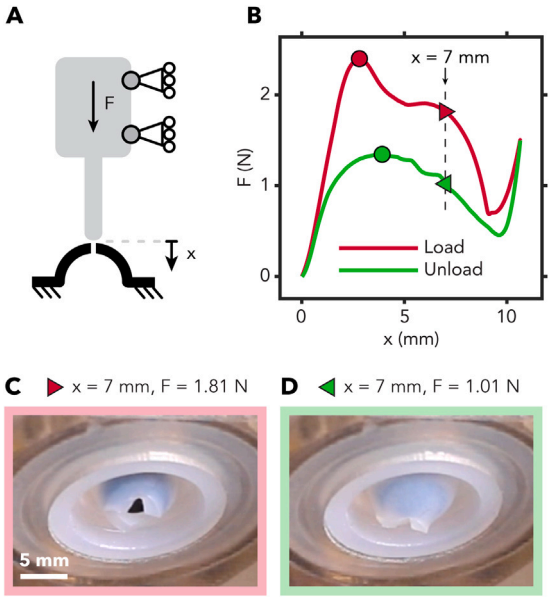

Fig. 10. Displacement-controlled loading experiment of the valve. (A) Schematic of the experimental setup. A custom probe is attached to a universal testing system (Instron), see Additional Fig. 21 for a detailed overview of the setup. (B) Measured force during loading (red curve) and unloading (green curve). Circular markers indicate local maxima, triangles mark an identical displacement value during loading (red, pointing right) and unloading (green, pointing left) for which we show the deformed valve in panels (C) and (D), respectively.

by forward integration of Eqs. (14) and (15) (Fig. 9). From this analysis, we see that the equilibrium transitions in a continuous manner from an unstable node to an unstable spiral, then in a supercritical Hopf bifurcation to a stable spiral, and finally to a stable node (Fig. 9B) (Khalil, 2002). The limit cycle disappears at the Hopf bifurcation, where the stable node appears (Fig. 9A). This conclusively shows that the initial system description can only explain the oscillation mode and not the regulation mode, as stability of the suspected regulation mode depends heavily on damping which is unphysical in comparison to our experiments.

5. Modified valve model

The initial model of the valve is based on the most basic spring-model that shows a snap-through instability (due to the compression spring), without being bistable at zero load, and an intuitive model for the conduction of air through the valve opening. In Section 4.3 we show that this model cannot explain the regulation mode. In the current section we aim to improve the model so that it will capture the observed behavior. Thereto, we revisit the experimental results and perform an additional experiment to understand what we are still missing in our model. We then update the model to reflect these insights and perform a similar analysis as we did for the initial model.

5.1. Definition of the modified model

When comparing the initial model with experiments, one important difference is the slope of the regulation mode in the Q_{out}–Δp plane (Fig. 6). Experimentally, we observe that the regulation mode has a positive slope, i.e., $\mathrm{d}\Delta p/\mathrm{d}Q_{\text{out}} > 0$, and this cannot be reproduced by the initial model. That is because the regulation mode is located at a displacement value that is characterized by negative differential stiffness $\mathrm{d}\Delta p/\mathrm{d}x < 0$, which requires $\mathrm{d}\Delta p/\mathrm{d}Q_{\text{out}} < 0$ for stability according to Eq. (32). We hypothesize that the experimentally observed positive slope of the regulation mode in the Q_{out}–Δp plane is essential and should be featured in a modified model. That implies that the regulation mode must be associated with positive differential stiffness, i.e., $\mathrm{d}\Delta p/\mathrm{d}x > 0$.

To qualitatively test if there exists another state (besides the fully open state) that has positive differential stiffness and where the valve is open, we conduct an experiment where we deform a valve with a probe (Fig. 10A). We control the position of the probe while monitoring the reaction force and the deformation of the valve. Despite the difference in loading conditions compared to loading with pressurized air, this experiment still provides important clues about the general mechanical behavior of the valve.

Specifically, that there are two distinct paths, during loading and unloading (Fig. 10B), and the difference seems too large to be explained from material dissipation alone. This is supported by the observed deformation (Figs. 10C and D). The shape of the valve during loading is symmetric (Fig. 10C), while the shape during unloading is asymmetric (Fig. 10D) and similar to the shape observed in the regulation mode (Fig. 1E(i) and Fig. 2D(i) – (iii)).

We recognize that these results may be influenced by the indenter. Especially along the loading path beyond the pressure maximum, the indenter seems to stabilize a symmetric deformed shape that may not be seen when the valve is loaded with air

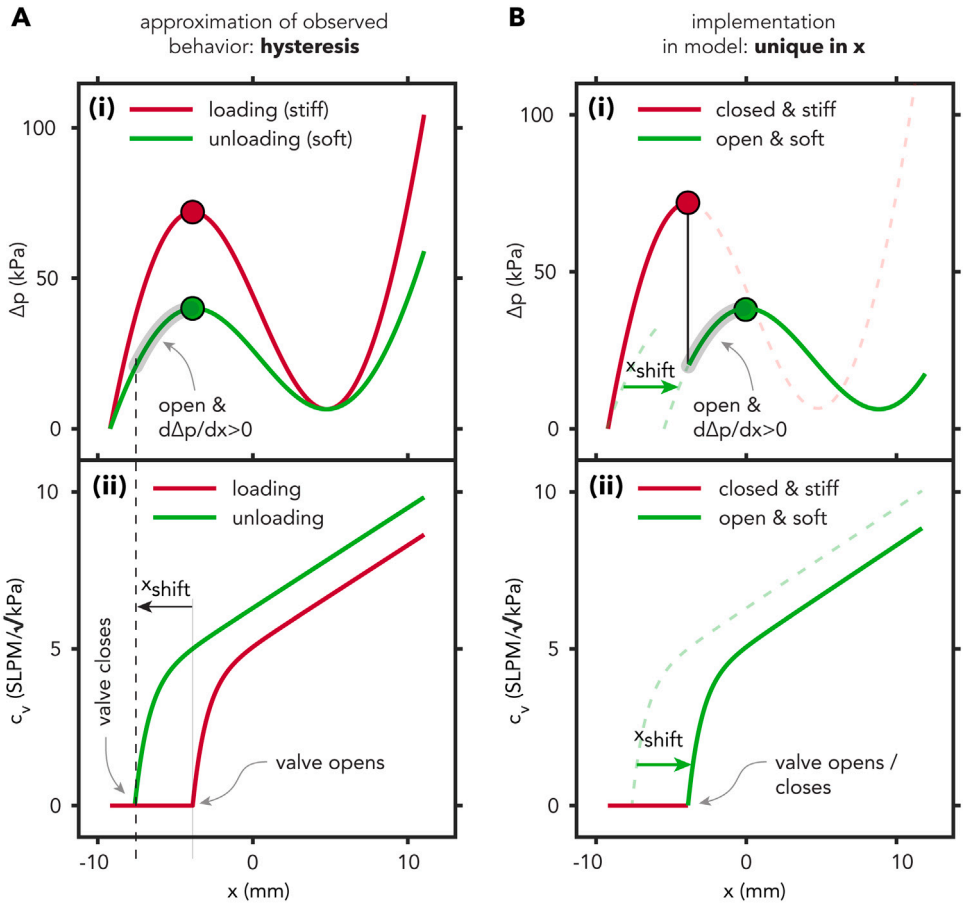

Fig. 11. A modified model to account for additional hysteresis in the mechanics and conduction behavior. (A) Idealization of the actual, observed behavior (see Fig. 10), with hysteresis in mechanics and valve conduction. (i) Equilibrium pressure difference over the valve as function of displacement of the dome. The loading curve (red) is stiffer than the unloading curve (green). At $x_{\text{open}} = x^{+}_{\text{snap, stiff}}$ the pressure-displacement curve switches between the stiff and soft curves. (ii) Valve conduction as function of displacement of the dome. During loading (red curve), the valve opens around the pressure maximum of the corresponding pressure-displacement curve (red circular marker in A(i)), but during unloading (green curve) the valve closes at a smaller displacement than the local maximum of the corresponding pressure-displacement curve (green circular marker in A(i)). (B) Modified model implementation. (i) The soft curve is shifted to the right. (ii) The unloading conduction curve is shifted on top of the loading curve.

pressure. We are led to this belief by experiments where we vary the maximum indentation distance, as shown in Additional Fig. 22. That experiment shows that when the valve is probed to sufficient displacement, representative of the case where the valve transitions from the fully open state to its initial shape, it follows the (green) unloading path shown in Fig. 10B.

Even if the loading path measured with a probe may not be fully representative of the hydrostatic load case, these observations indicate there is hysteresis under displacement control that we do not take into account in our initial model. To represent this finding, we define an idealized description of the observed behavior with a stiffer loading curve and a softer unloading curve, as shown schematically in Fig. 11A(i) and we define $x^{+}_{\text{snap, stiff}}$ of the stiffer curve as the point where the valve switches between the two curves during loading. During unloading, the softer path is followed. Since the valve follows different paths during loading and unloading, the valve orifice does not need to close upon unloading at the same displacement value where it opens upon loading. Crucially, such hysteresis in the valve conduction may result in the existence of the required displacement range where the valve is open, and differential stiffness is positive (gray highlight in Fig. 11A(i)). As an idealized description of this conduction behavior, we assume two identical conduction curves, modulo a certain (as of yet unknown) translation x_{shift}, as shown schematically in Fig. 11A(ii).

However, explicitly implementing even this highly simplified additional hysteresis behavior complicates the model, because both c_{v} and p_{S} are no longer functions of x. We prefer to maintain a uniquely defined model in x, and to keep the number of DOFs in our model to a minimum, while still introducing this potentially crucial additional behavior. To obtain this result, we firstly ensure that the conduction behavior is uniquely defined. Thereto, we translate the conduction curve associated with unloading by $-x_{\text{shift}}$, such that it overlaps with the conduction curve associated with loading (Fig. 11B(ii)). Secondly, to maintain the assumed relation between pressure and valve conduction, we translate the softer mechanical curve by the same amount (Fig. 11B(i)). Note that the

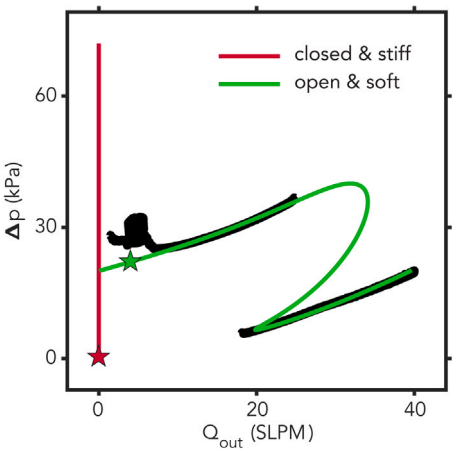

Fig. 12. Nullcline $dx/dt = 0$ of the modified model. The red line corresponds to the stiffer behavior for $x \leq x_{\text{open}}$, where the valve is closed. The green curve corresponds to the softer behavior at $x > x_{\text{open}}$, where the valve is open. The nullcline fits measured values $\Delta p(Q_{\text{out}})$ (black curves) both in the regulation mode and in the fully open state. Parameter values are listed in Table 2.

Table 2
Parameters used for the stability analysis of the modified model.

Parameter	Value	Unit
b_0	12	mm
h_0	9.2	mm
θ	75	deg
A_v	452.4	mm^2
k_S	3.0×10^7	N mm^{-1}
k_R	3.7×10^8	N mm rad^{-1}
$k_{S,\text{soft}}$	1.6×10^7	N mm^{-1}
$k_{R,\text{soft}}$	2.2×10^8	N mm rad^{-1}
C_0	0.06	1/60SL/kPa
x_{open}	−3.9	mm
x_{shift}	3.7	mm
ψ	1.1	mm^{-1}
c_i	3.9	$\text{SLPM}/\sqrt{\text{kPa}}$
s_∞	0.3	$\text{SLPM}/\sqrt{\text{kPa}}/\text{mm}$

value of x_{shift} will later be determined from a fit to experimental data. This procedure artificially makes the relevant part of the unloading curve accessible, without introducing additional hysteresis.

The modified model is described by the same differential equations (Eqs. (14) and (15)) and conduction model (Eq. (13)) as the initial model. The spring model is piece-wise identical to the initial definition of Eq. (8), i.e.,

$$F_{S,\text{ mod}} = \begin{cases} F_S(x), \quad k_S = k_{S,\text{stiff}}, k_R = k_{R,\text{stiff}} & x \leq x_{\text{open}} \\ F_S(x - x_{\text{shift}}), \quad k_S = k_{S,\text{soft}}, k_R = k_{R,\text{soft}} & x > x_{\text{open}}, \end{cases} \tag{36}$$

where we leave the stiffer curve unchanged with respect to the initial model. We introduce three new variables $k_{S,\text{soft}}$, $k_{R,\text{soft}}$ and x_{shift} that describe the softer curve. We link their values to experimental observations as follows. First, we take the values of $k_{S,\text{soft}}$ and $k_{R,\text{soft}}$ such that the local pressure minimum is equal to the value Δp_{close} found in a static experiment ($\Delta p_{\text{close}} \approx 5\,\text{kPa}$, see Fig. 3), so $p^-_{\text{snap,soft}} = p^-_{\text{snap, stiff}} = \Delta p_{\text{close}}$. Then, for different values of $p^+_{\text{snap,soft}}$ we determine the values of x_{shift} and valve conduction parameters ψ, s_∞ and c_i that minimize the least-squares error between model and experimental data. We visually observe that a good fit is obtained for $p^+_{\text{snap,soft}} = 40\,\text{kPa}$.

The resulting nullcline $dx/dt = 0$ is shown in Fig. 12, alongside measured data. The modified model allows a good fit to data both in the fully open state and in the regulation mode. Importantly, the modified model results in the existence of a displacement range with positive slope $\partial \Delta p / \partial Q_{\text{out}} > 0$. Note that we develop our model based on measurements of the regulation mode for inflow rates $Q_{\text{in}} \leq 25\,\text{SLPM}$, which is a limitation of our mass flow control equipment. At $Q_{\text{in}} = 25\,\text{SLPM}$, the valve is still in the regulation mode, but the model predicts that the valve must transition from the regulation mode to the fully open state if we increase the flow rate even further (Fig. 12). For completeness, we qualitatively verify this prediction, by connecting the valve directly to a pressure regulator, while we measure pressure before and behind the valve and flow through the valve (Additional Fig. 20). That is the same setup we use to measure the fully open state at higher flow rates (green curve in Fig. 3). Interestingly, we observe not only the transition to the open state, but even the pressure decrease before the transition, although we continue to manually increase the pressure setpoint. The pressure drop is able to decrease while we increase the setpoint, because there is restriction

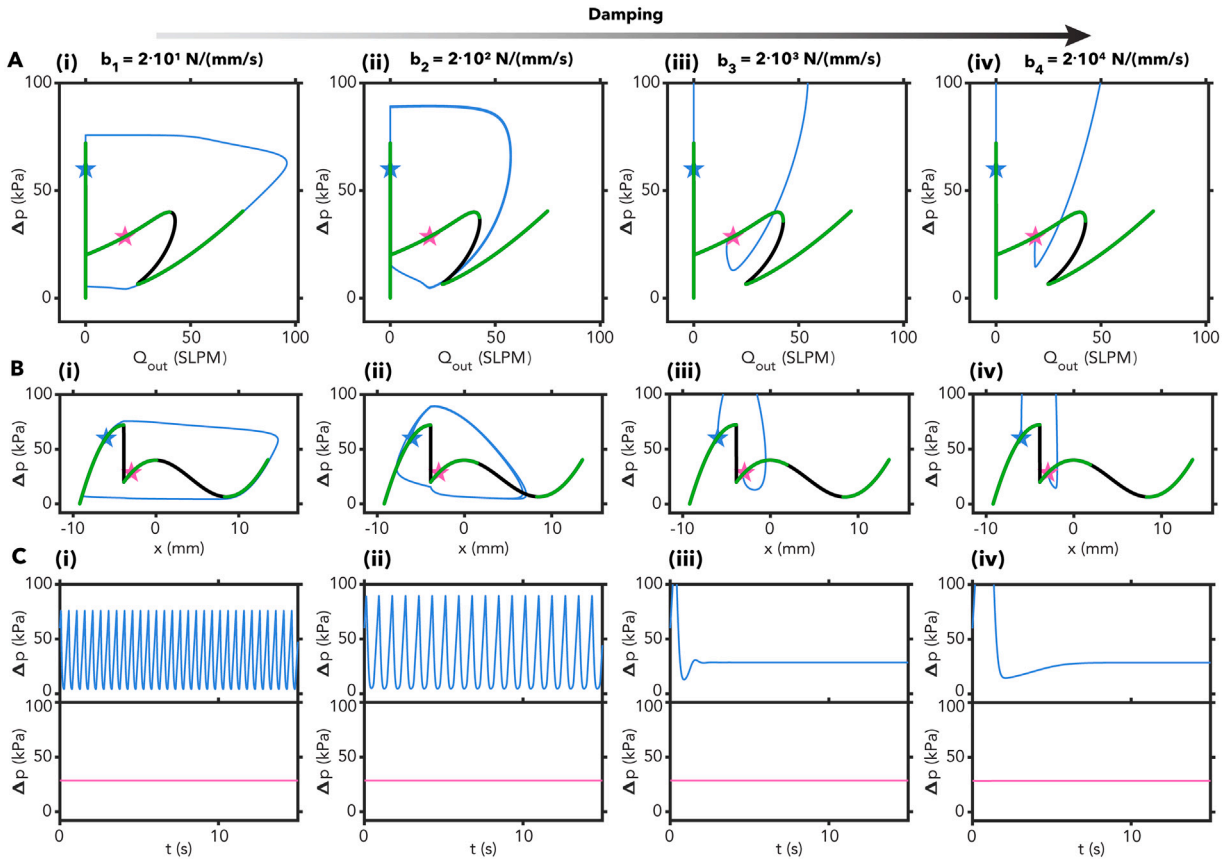

Fig. 13. Simulated effect of damping parameter b on the dynamic response of the modified model. (A) and (B) Simulated trajectories (blue and magenta curves) for two different initial conditions (blue and magenta stars) and $Q_{\text{in}} = 15\,\text{SLPM}$, shown in the Q_{out}–Δp plane (A), and in the x–Δp plane (B). Black curves represent the nullcline $\mathrm{d}x/\mathrm{d}t = 0$, where green overlay corresponds to stable equilibria. (C) Simulated pressure difference Δp over the valve for the same trajectories shown in (A) and (B). Columns (i) to (iv) show results for increasing values of b, as indicated. Parameter values are listed in Table 2.

(tubes, connectors) between the pressure regulator and the valve, such that this setup approximates flow control rather than pure pressure control. The extended experiment qualitatively verifies the final part of the nullcline that was not observed at lower flow rates in the experiments using a dedicated flow controller (black curve in Fig. 3).

5.2. Coexistence of regulation and oscillation in the modified model

To determine if the modified model can explain coexistence of the regulation mode and the oscillation mode, we numerically analyze the effect of damping parameter b, as we did for the initial model. In Fig. 13 we show the system response for four values of damping, and for a constant inflow rate $Q_{\text{in}} = 15\,\text{SLPM}$.

Crucially, and differently from the initial model, at any of the studied values of damping there exists a stable equilibrium for a wide range of inflow rates, specifically for any inflow rate where $\partial p_S/\partial x > 0$. For increasing damping values, the stable range of inflow rates grows to include also the part where $\partial Q_{\text{out}}/\partial p_S < 0 \wedge \partial p_S/\partial x < 0$. Similarly to the initial model, we observe a limit cycle that corresponds to the oscillation mode. Increasing damping affects the oscillation mode. Higher damping slows down the transitions between open and closed states, which increases Δp_{open}, and decreases the cycle frequency (i) and (ii). As in the initial model, the oscillation mode disappears altogether at high damping (iii) and (iv). Excitingly, the modified model thus reproduces the coexistence of the oscillation and regulation mode (for moderate values of the damping parameter).

In the modified model, the oscillation mode is surrounding a stable equilibrium. Therefore, for the stable limit cycle to exist, there must also exist an unstable limit cycle between the stable regulation mode and the stable oscillator. To probe the existence of such unstable limit cycle, we integrate differential equations Eqs. (14) and (15) both forward and backward in time, where we use the modified model Eq. (36) for the mechanics. We start from initial conditions near the expected limit cycle, near the stable equilibrium, and in between.

In Fig. 14A we show stable (gray) and unstable (red) limit cycles for different values of b. At lower damping values, we find a single unstable limit cycle between the stable oscillating and regulation modes, as required for the coexistence of both modes. Interestingly, both limit cycles deform for increasing damping, until at $b \approx 220\,\text{N s mm}^{-1}$ they disappear in a fold of limit cycles.

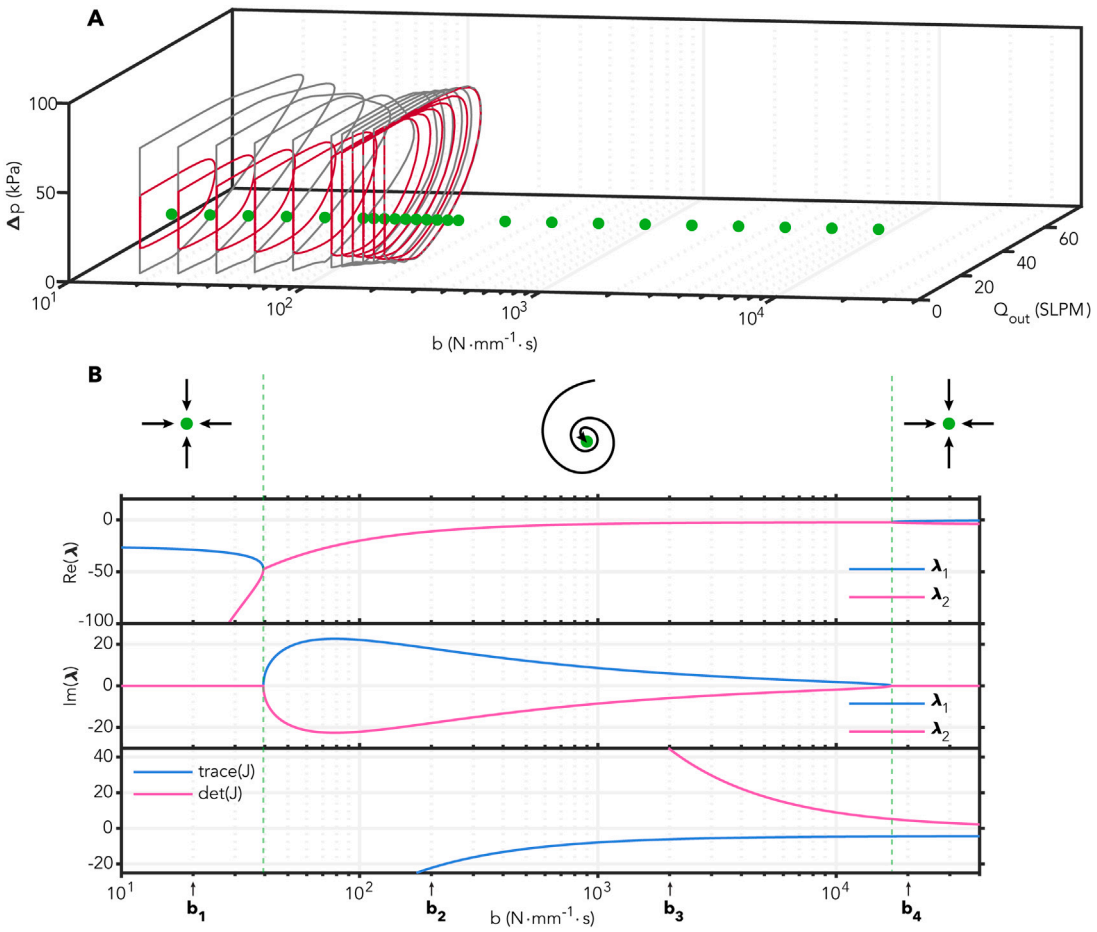

Fig. 14. Simulated effect of damping on stability of oscillation and regulation modes in the modified model, for Q_{in} = 15 SLPM. (A) Stable (gray curves) and unstable (red curves) limit cycles in the Q_{out}–Δp plane for different values of damping b. For all values of b, the single equilibrium is stable (green marker). (B) Real and imaginary parts of the eigenvalues of the Jacobian and trace and determinant of the Jacobian. Flow symbols indicate (from left to right) stable node, stable spiral, stable node. Parameter values are listed in Table 2.

This is in contrast to the situation in the initial model, where the oscillation mode disappeared in a Hopf bifurcation, giving rise to the regulation mode. In the modified model, the regulation mode transforms from a stable node to a focus and back for increasing damping values, but never becomes unstable (Fig. 14B).

Having determined the coexistence of regulation and oscillation, as well as the effect of damping, we can now try to replicate key results observed in experiments. Firstly, recall that the system can enter the regulation mode as a result of a disturbance (Fig. 1). In the experiment we temporarily pinch a tube behind the valve. In our numerical replication of the experiment, we approximate this disturbance by temporarily increasing damping parameter b (Fig. 15A). This causes the system to transition from the oscillation mode to the regulation mode. That is because increased damping temporarily removes the oscillation mode, conform Figs. 13 and 14. The system is therefore attracted to the regulation mode. Once in the regulation mode, the system stays in that mode even when the damping value is restored to its original value, because it is now inside the unstable limit cycle that separates the two modes.

Secondly, recall that upon varying the inflow rate over a wide range in an experiment, the system remains in the mode in which it started (Fig. 2). Numerically, we similarly apply a varying inflow rate (Fig. 15B(i)) and first start the system from an initial condition corresponding to the regulation mode (green star in Fig. 15B(ii)). As in the experiment, the system remains in the regulation mode as the flow rate is increased and decreased. Differently from the experiment, the simulated system does not exit the regulation mode until the flow completely stops. Then, we start from an initial condition corresponding to the oscillation mode (red star in Fig. 15B(iii)). The simulated system continues to oscillate when the inflow rate is changed. The oscillation frequency first increases, then decreases until the system stops oscillating as it enters the fully open state. Upon decreasing the inflow rate the system restarts oscillating at the same inflow rate where it stopped.

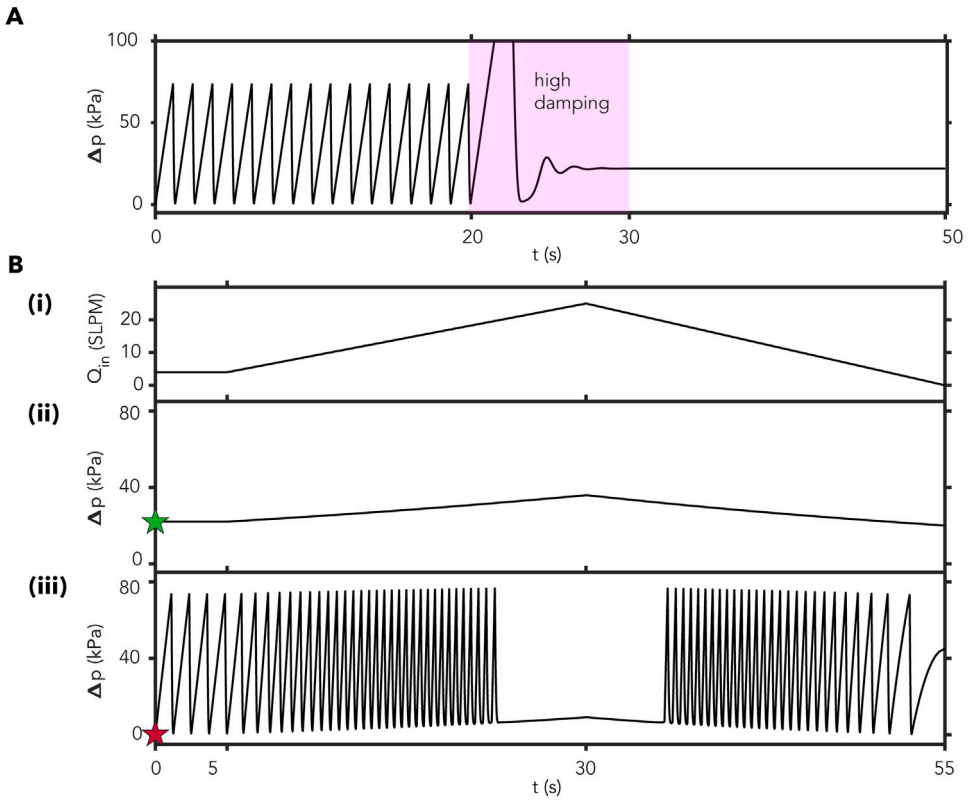

Fig. 15. Numerical replication of experimental results. (A) A temporary disturbance permanently moves the system from the oscillation to the regulation mode (compare to the experiment in Fig. 1). Simulated pressure difference Δp for a constant inflow rate $Q_{\text{in}} = 4\,\text{SLPM}$. $b = 20\,\text{N s mm}^{-1}$ for the first twenty seconds, $b = 1 \times 10^4\,\text{N s mm}^{-1}$ between $t = 20\,\text{s}$ and $t = 30\,\text{s}$, then $b = 20\,\text{N s mm}^{-1}$ again. (B) The system remains in regulation or oscillation mode for a wide range of inflow rates (compare to the experiment shown in Fig. 2). (i) Inflow rate $Q_{\text{in}} = 4\,\text{SLPM}$ in the first five seconds, then increases to $Q_{\text{in}} = 25\,\text{SLPM}$ at $t = 30\,\text{s}$, and decreases to $Q_{\text{in}} = 0$ at $t = 55\,\text{s}$. (ii) and (iii) Simulated pressure difference Δp for $b = 20\,\text{N s mm}^{-1}$, when starting from initial conditions close to the regulation mode (ii) or oscillation mode (iii). Parameter values are listed in Table 2.

6. Suppressing the regulation mode

The modified model provides a mechanistic explanation for the existence of the regulation mode. In the remainder of this work, we will test the predictive power of the model by using it as a design tool to avoid the existence of the regulation mode. This goal is motivated by the application of hysteretic valves in soft robot control, where the existence of the regulation mode could in some cases be a risk. As we have seen, the system can enter this mode by temporary disturbances, that may not always be avoidable.

Of several available routes to avoid regulation, here we focus on changing only the valve conduction behavior, without significantly changing the mechanics. The regulation mode exists at low flow rates because it maintains a large enough pressure drop to prevent the valve from snapping back to its initial state (Figs. 1B and 2B). This is possible because the valve orifice is almost completely closed (Fig. 1E(i) and 2D(i)–(iii)). This prompts us to study what happens when the valve never completely closes, except in its initial state.

In Fig. 16 we show an implementation of this concept in our model. We study the effect on the nullclines when we assume that a finite orifice opening remains for all $x > x_{\text{open}}$. In the initial state, the valve is still completely closed, i.e., $c_{\text{v}} = 0$ for $x \leq x_{\text{open}}$. We implement the inhibition of premature closing by adding a factor ρ to our definition of the valve conduction

$$c_{\text{v}} = \begin{cases} 0 & x \leq x_{\text{open}} \\ \rho\, c_{\text{i}} + (1-\rho)\, c_{\text{i}} \left(1 - e^{\psi\left(x_{\text{open}} - x\right)}\right) + s_{\infty}\,(x - x_{\text{open}}) & x > x_{\text{open}}. \end{cases} \tag{37}$$

In Fig. 16A we show the resulting conduction behavior, and in Fig. 16B we show the effect on the nullcline $\mathrm{d}x/\mathrm{d}t = 0$. Varying parameter ρ between 0 and 1, i.e., increasing the minimum conduction value from 0 to 1 times c_{i}, results in the disappearance of equilibria in the range $0 < Q_{\text{in}} < Q^{-}_{\text{reg}}$, where

$$Q^{-}_{\text{reg}} = c_{\text{v}}(x_{\text{open}})\sqrt{p_{\text{S}}(x_{\text{open}})} = \rho\, c_{\text{i}}\sqrt{p_{\text{S}}(x_{\text{open}})}, \tag{38}$$

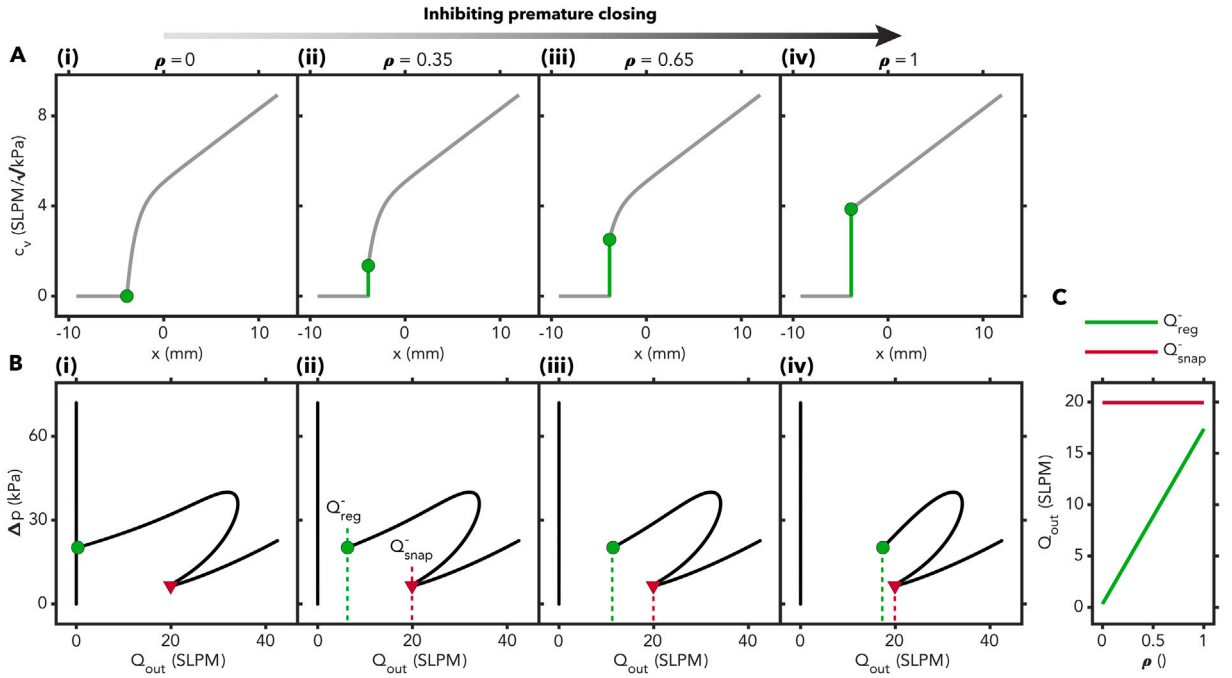

Fig. 16. Avoiding regulation by avoiding complete closure of the valve. (A) The effect of design parameter ρ on valve conduction. For increasing values of ρ, valve closure in the open state is increasingly inhibited. $\rho = 0$ represents the original valve design where the valve closes completely before snapping back to the fully closed state, $\rho = 1$ nullifies the effect of ψ and maximizes the discontinuous jump at x_{open}. Green circular markers indicate conduction value $c_v(x_{\text{open}}) = \rho\, c_i$ at valve opening and closing. Green lines indicate a jump. (B) Effect of ρ on nullcline $\mathrm{d}x/Dt = 0$. Green circular markers correspond to outflow rate Q^-_{reg} at valve opening and closing. Red triangles correspond to the local flow rate minimum Q^-_{snap} (associated with the local pressure minimum Δp^-_{snap}). (C) Evolution of Q^-_{reg} and Q^-_{snap} as function of ρ.

such that Q^-_{reg} increases linearly with ρ (Fig. 16C). Setting $\rho = 1$ all but completely suppresses the coexistence of the oscillating and regulation modes. From an application perspective, Q^-_{reg} is a safe maximum operating inflow rate, below which the regulation mode cannot exist.

To experimentally validate this predicted behavior, we fabricate a valve that has additional features aimed at preventing the valve from closing completely when it is in the regulation mode. Thereto, the valve has protrusions on the convex side of the dome, around the cut. Moreover, instead of three shorter slits, we cut a single longer slit, as shown in Figs. 17A(i) and (ii). The detailed design is shown in Additional Fig. 18. We conduct an experiment where we first increase the flow rate from $Q_{\text{in}} = 0$ to $Q_{\text{in}} = 20$ SLPM in 70 s. We observe that the valve enters the fully open state at $Q_{\text{in}} = 10$ SLPM (light gray star in Fig. 17A(iii)). While we hold the flow rate at $Q_{\text{in}} = 20$ SLPM, we physically push the valve, causing it to enter the regulation mode (gray star). Excitingly, when we then decrease the flow rate, the modified valve exits the regulation mode and restarts oscillations around the same inflow rate (black star) where it entered the open state. This means that there is no longer coexistence between the regulation mode and the oscillation mode at any flow rate, demonstrating the validity of the model-based prediction.

As a reference, in Fig. 17B we show results of the same experiment using the original valve design. The valve enters the fully open state at $Q_{\text{in}} = 18$ SLPM, which is higher than the modified valve. Again, we physically push the valve, causing it to enter the regulation mode (gray star). When we decrease the flow rate, the valve remains in the regulation mode until $Q_{\text{in}} = 2$ SLPM (black star), as expected from the other experimental evidence (e.g., Fig. 2).

These results demonstrate that we can prevent the valve from closing completely in the regulation mode, which in turn removes the existence of the regulation mode at lower flow rates, as predicted by the model. This high-level result is summarized in Fig. 17D, where we show the inflow rates for which the oscillation mode, the regulation mode, and the fully open state exist for the two valve designs. Note that, besides the desired effect, modifying the design also causes the valve to enter the fully open state at a significantly lower flow rate compared to the original design. The model did not predict this decrease of the maximum flow rate for the oscillation mode as a result of changing ρ. In reality, the modifications to the design do not only change the fluidics, but also affect the mechanics to some extent, resulting in a decrease of p^-_{snap}. We measure a pressure drop at closing of the valve $\Delta p_{\text{close}} \approx 0$, indicating that the modified valve is nearly bistable. In future work, this could potentially be mitigated by also changing mechanical parameters (thickness, dome angle).

7. Discussion

The goal of the present study is to understand the coexistence of a pressure regulation mode and an oscillation mode in soft hysteretic valves, and more generally to better describe the mechanics and dynamics of the valve in a fluidic circuit. In previous

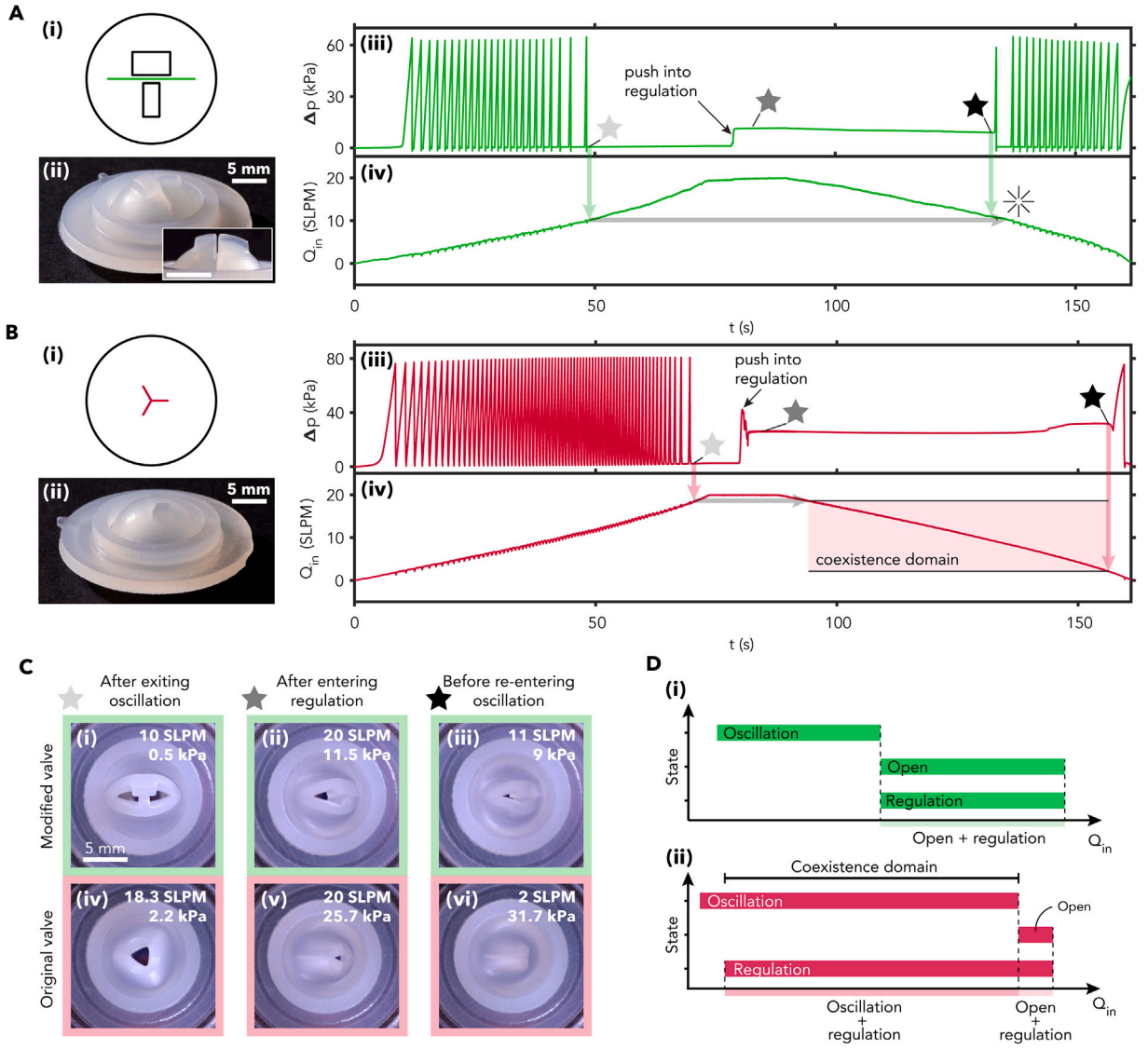

Fig. 17. Experimental realization of suppression of the regulation mode. (A) The modified valve. (i) Sketch of top view (green line: laser-cut slit), and (ii) oblique view photograph. The inset shows a side view of the protrusions and the slit (scale bar 5 mm). (iii) Measured pressure drop Δp over the valve, and (iv) measured inflow rate Q_{in}. There are no inflow rates for which the regulation and oscillation mode coexist. Star symbols refer to panel C. (B) The original valve. (i) Sketch of top view (red line: laser-cut slit), and (ii) oblique view photograph (scale bar 5 mm). (iii) Measured pressure drop Δp over the valve, and (iv) measured inflow rate Q_{in}. Red shaded area indicates the flow rates for which the regulation and oscillation mode coexist. Star symbols refer to panel C. (C) Observed states of the modified and original valve. (D) Flow rates for which the (i) modified and (ii) original valve can be in each of three states, the oscillation mode, regulation mode or fully open state. (i) Green bars indicate for each mode at which range of flow rates the modified valve can be in that mode, showing no overlap between oscillation and regulation. (ii) Red bars indicate for each mode at which range of flow rates the original valve can be in that mode, showing significant overlap between oscillation and regulation.

work, we model the same valves as pressure-controlled switches that can be either in a fully open, or a fully closed state (Van Laake et al., 2022). Using that approach we can, by definition, only describe the behavior of the valve in the oscillation mode and the fully closed and open states. Therefore, in the present work, we aim to develop a more complete, but minimal model that captures also the regulation mode.

We conclude from our analysis that an essential feature to explain the coexistence of the regulation and oscillation modes at the same inflow rate and realistic damping values is the existence of a displacement range with positive differential stiffness. Moreover, the regulation mode relies on near-complete closure of the orifice, which we can prevent by changing the valve design. Taken together, our analysis provides a mechanistic explanation of the observed behavior, and can be used for informed design change decisions.

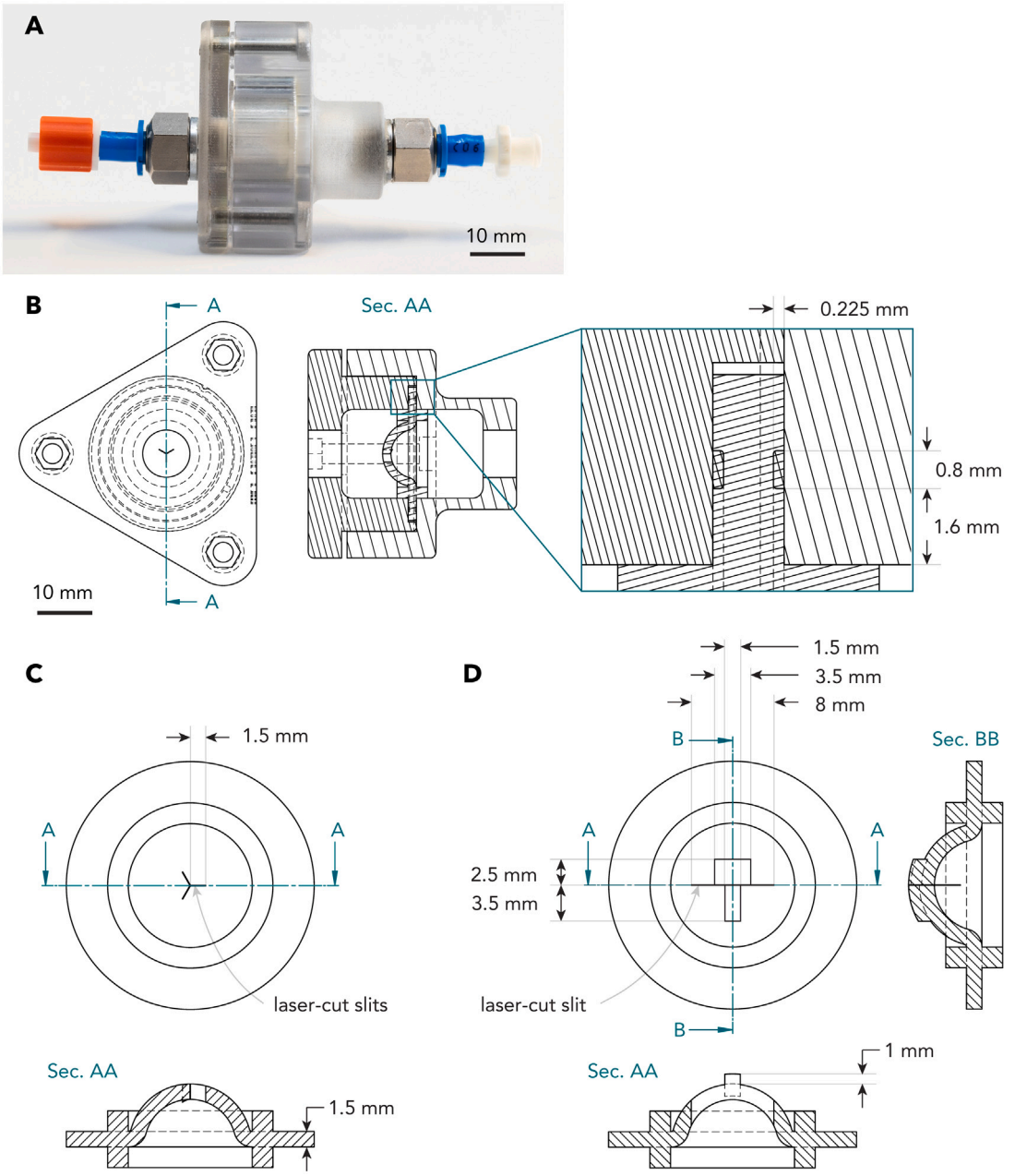

Fig. 18. Valve and holder designs. (A) Assembled valve holder. (B) Valve holder design. (C) Original valve design (uniformly scaled up by a factor two with respect to the design used in our previous work (Van Laake et al., 2022)). (D) Modified valve design.

This work is limited to a specific valve design, of which we change the fluidic characteristics in order to remove the regulation mode at low flow. However, we conclude that specifics of the mechanics are also essential for the existence of the regulation mode. Therefore, in future work, it will be interesting to study the effect of the undeformed shape of the valve, such as the thickness and shallowness of the dome, as well as its boundary conditions.

Furthermore, in this work, we neglect visco-elastic effects, although visco-elasticity may cause some detailed effects that we currently do not capture in our model. For example, our model predicts a continuous increase of Δp_{open} for increasing Q_{in} (Fig. 15). In experiments, we see that Δp_{open} initially increases, then decreases (Fig. 2). We hypothesize that this is caused by a memory effect. At higher flow rates, the valve remains longer in the open state before snapping back (T_{open} increases), such that it increasingly relaxes in that deformation state. At the same time, the valve spends less time in its initial state (T_{close} decreases). The net outcome could be an increased effect of residual stress on the forward snap-through event, which results in a lower effective Δp_{open}. A better

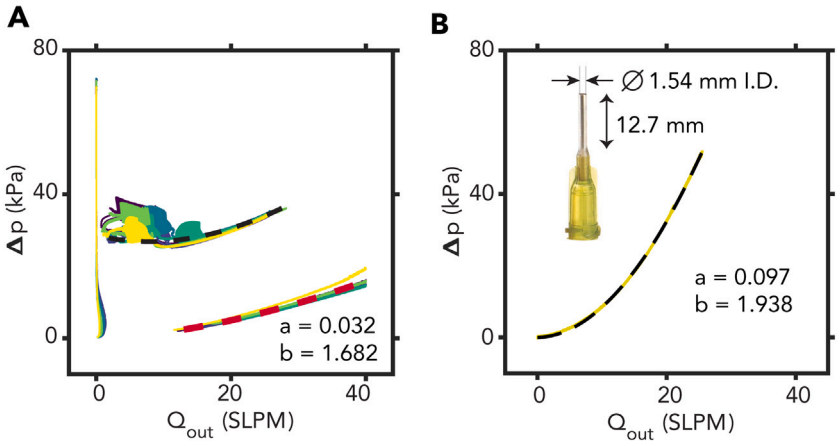

Fig. 19. Pressure drop over the valve, compared to pressure drop over constant orifices. In (A) and (B) a and b are fitting parameters, for the fitting function $\Delta p = a\,(Q_{\text{out}})^b$. (A) Measured pressure drop Δp over the valve, as function of flow rate Q_{out} obtained in quasi-static experiments, under pressure control for the fully open state, and under flow control in the regulation mode. Different colors refer to six specimens of the same valve design. a and b are mean fitting parameters for six valves, for the open state behavior. (B) Measured pressure drop Δp over a needle (length $L = 1.27\,\text{mm}$, internal diameter $D = 1.54\,\text{mm}$), as function of flow rate Q_{out}, obtained in a quasi-static experiment under flow control.

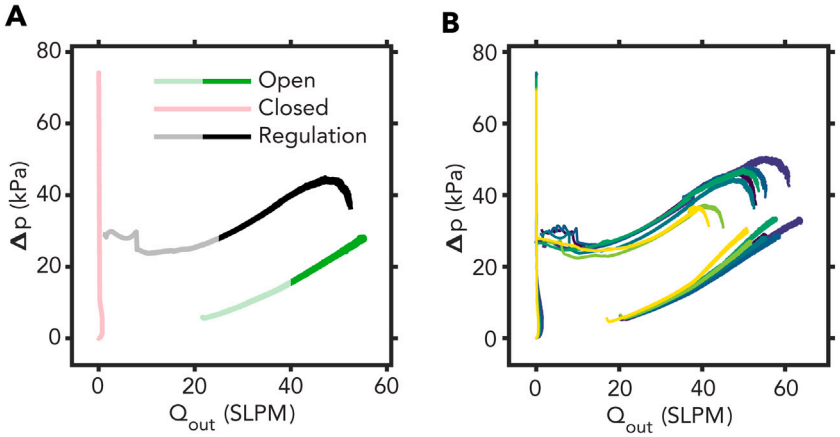

Fig. 20. Experiment of quasi-static pressure drop as function of outflow rate $\Delta p(Q_{\text{out}})$ for extended range of flow rates compared to Fig. 3. (A) One representative sample. All curves, i.e., the closed (light red curve) and fully open (light and solid green curves) states, as well as pressure regulation mode (light and solid black curves) are obtained in the same quasi-static experimental setup using a pressure regulator connected to the valve holder. Solid black and green data represent extended flow rate range. (B) Seven samples.

understanding of this relation could be valuable in applications where small imperfections between multiple valves affect activation patterns of multiple actuators (Van Laake et al., 2022).

We focus on the development of a minimal model, ultimately geared towards promoting one or the other mode in our hysteretic valves. However, we notice that our system shows behavior that may be interesting for more fundamental future studies, as well. The valve in its oscillating mode slows down considerably as we increase the inflow rate, until it stops oscillating. Potentially, our valve could provide an interesting platform for studying dynamics around critical points (Gomez et al., 2017).

Finally, we note that circuits with hysteretic valves, and fluidic circuits in general, are increasingly used to control fluid-driven soft robots (Vasios et al., 2020; Van Laake et al., 2022; Park et al., 2022; Jin et al., 2023; Mahon et al., 2019; Hubbard et al., 2021; Song et al., 2021; Hoang et al., 2021; Napp et al., 2014; Park et al., 2022; Teichmann et al., 2023; Zhai et al., 2023; Rothemund et al., 2018; Drotman et al., 2021; Decker et al., 2022; Overvelde et al., 2015; Van Raemdonck et al., 2023; Wehner et al., 2016; Gorissen et al., 2020). Multidisciplinary studies (mechanics, fluidics, and dynamics) like the present one, may contribute to better understanding of system-level behavior in such fluidic circuits. For example, a bistable valve that can create fluidic oscillations from a continuous (pressure) input has been observed to stop oscillating under certain conditions, like our valve (Rothemund et al., 2018). The methods and models developed in the present work may provide insights into that behavior, or can otherwise at least indicate which kind of additional experiments should be performed to better explain its fundamentals. This is especially important in the field of soft robotics, where embodied intelligence and safe interaction with humans are important claimed benefits, while formal robustness and other performance criteria are still underdeveloped. As a result of the present study, we better understand

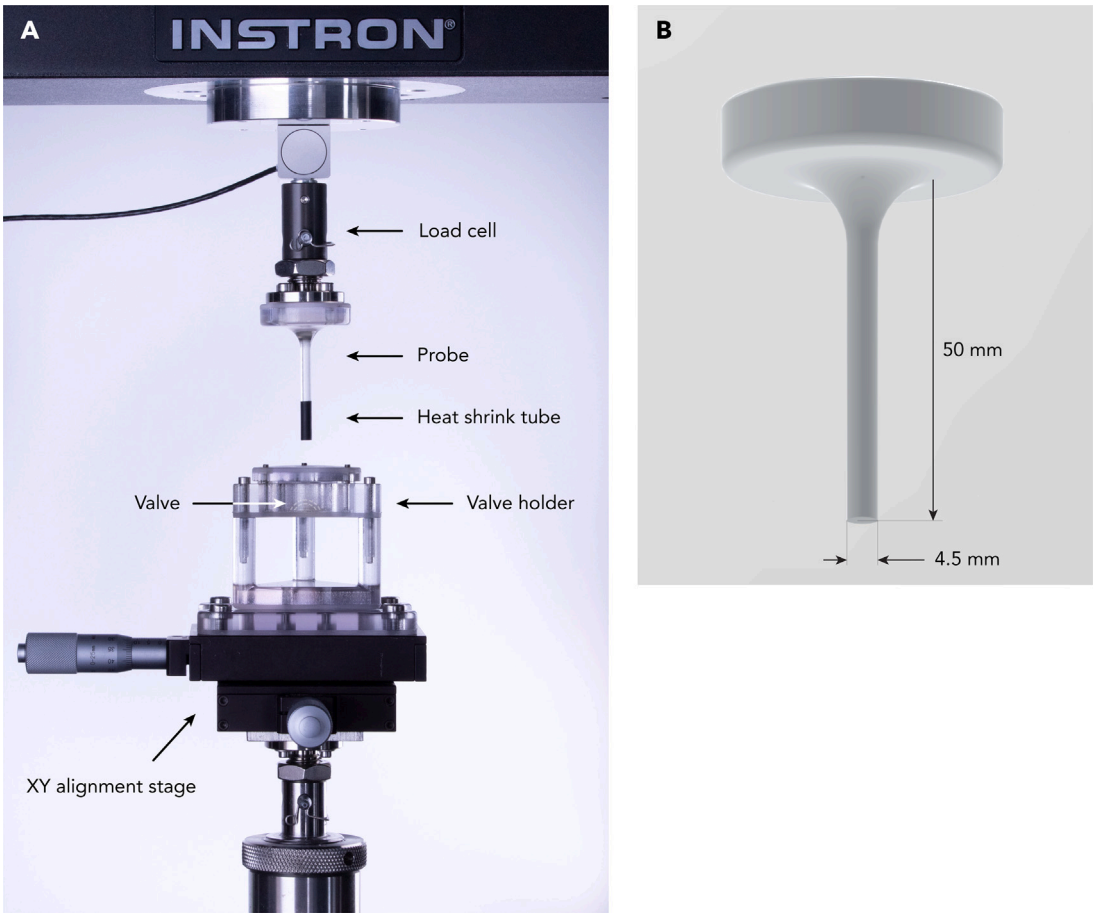

Fig. 21. Experimental setup for probing valve hysteresis. (A) overview of the setup. The valve (not visible) is mounted inside the holder with its convex side up. The holder and probe are 3D-printed (VeroClear, Stratasys). The probe is fitted with a length of shrink tube to increase friction. (B) Probe design.

stability criteria of the regulation mode in a specific type of hysteretic valves. This may contribute to the reliability of future soft robotic applications such as autonomous walking robots, and medical prosthetic devices.

CRediT authorship contribution statement

Lucas C. van Laake: Conceptualization, Data curation, Formal analysis, Investigation, Methodology, Software, Supervision, Validation, Visualization, Writing – original draft, Writing – review & editing. **Alberto Comoretto:** Data curation, Formal analysis, Investigation, Methodology, Software, Validation, Visualization, Writing – review & editing. **Johannes T.B. Overvelde:** Conceptualization, Formal analysis, Funding acquisition, Methodology, Project administration, Resources, Supervision, Validation, Visualization, Writing – review & editing.

Declaration of competing interest

The authors declare that they have no known competing financial interests or personal relationships that could have appeared to influence the work reported in this paper.

Data availability

We have uploaded the data packages on Zenodo, The doi for the data is http://dx.doi.org/10.5281/zenodo.10693369.

Acknowledgments

This project has received funding from the European Union's Horizon 2020 research and innovation programme under grant agreements No 767195 and No 948132. This work is part of the Dutch Research Council (NWO) and was performed at the research institute AMOLF.

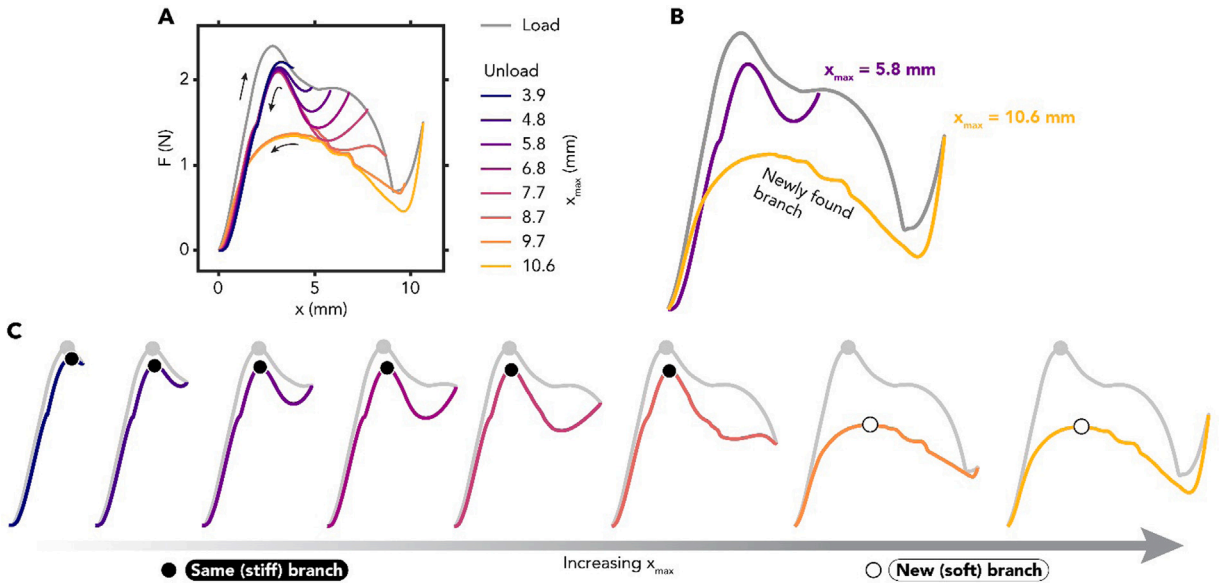

Fig. 22. Displacement-controlled loading experiment of the valve, where we vary the maximum displacement $x_{\max}$ of the probe. (A) Measured reaction force F as function of probe displacement x for different values of $x_{\max}$. A single representative loading curves (gray) is for all values of $x_{\max}$ overlap, unloading curves are colored by $x_{\max}$ according to the legend. (B) Loading curve (gray) and two representative unloading curves, one for probing with low displacement (purple), and one for high displacement (yellow). (C) Full loading/unloading trajectories for increasing values of $x_{\max}$ (from left to right). Circular markers indicate local maxima.

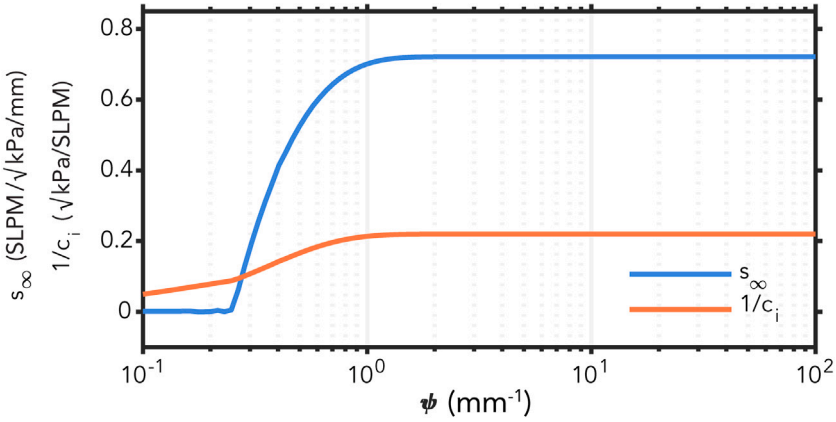

Fig. 23. For different values of x_{open} and ψ, we determine c_{i}, and s_∞ by fitting to measured values $\Delta p(Q_{\text{in}})$. Here, we show the resulting values for the (inverse) valve conduction $1/c_{\text{i}}$ ($\sqrt{kPa}$/SLPM), and slope s_∞ (SLPM/$\sqrt{kPa}$/mm) for $x_{\text{open}} = 1$ mm.

Appendix. Additional figures

See Figs. 18–23.

References

Abbasi, A., Yan, D., Reis, P.M., 2021. Probing the buckling of pressurized spherical shells. J. Mech. Phys. Solids 155 (June), 104545. http://dx.doi.org/10.1016/j.jmps.2021.104545.

Arfaee, M., Vis, A., Kluin, J., 2022. Future technologies in total artificial heart development: can a robot become as good as a donor heart? Eur. Heart J. 1–3. http://dx.doi.org/10.1093/eurheartj/ehac512.

Brinkmeyer, A., Santer, M., Pirrera, A., Weaver, P.M., 2012. Pseudo-bistable self-actuated domes for morphing applications. Int. J. Solids Struct. 49 (9), 1077–1087. http://dx.doi.org/10.1016/j.ijsolstr.2012.01.007.

Brown, P.E., 1995. United States Patent : 5861366 DISPENSING VALVE FOR PACKAGING.

Champneys, A.R., Dodwell, T.J., Groh, R.M., Hunt, G.W., Neville, R.M., Pirrera, A., Sakhaei, A.H., Schenk, M., Wadee, M.A., 2019. Happy catastrophe: Recent progress in analysis and exploitation of elastic instability. Front. Appl. Math. Stat. 5 (July), 1–30. http://dx.doi.org/10.3389/fams.2019.00034.

Decker, C.J., Jiang, H.J., Nemitz, M.P., Root, S.E., Rajappan, A., Alvarez, J.T., Tracz, J., Wille, L., Preston, D.J., Whitesides, G.M., 2022. Programmable soft valves for digital and analog control. Proc. Natl. Acad. Sci. 119 (40), 1–10. http://dx.doi.org/10.1073/pnas.2205922119.

Drotman, D., Jadhav, S., Sharp, D., Chan, C., Tolley, M.T., 2021. Electronics-free pneumatic circuits for controlling soft-legged robots. Science Robotics 6 (51), http://dx.doi.org/10.1126/SCIROBOTICS.AAY2627.

Evkin, A.Y., Lykhachova, O.V., 2019. Design buckling pressure for thin spherical shells: Development and validation. Int. J. Solids Struct. 156–157, 61–72. http://dx.doi.org/10.1016/j.ijsolstr.2018.06.035.

Gomez, M., Moulton, D.E., Vella, D., 2017. Critical slowing down in purely elastic 'snap-through' instabilities. Nat. Phys. 13 (2), 142–145. http://dx.doi.org/10.1038/nphys3915.

Gomez, M., Moulton, D.E., Vella, D., 2019. Dynamics of viscoelastic snap-through. J. Mech. Phys. Solids 124, 781–813. http://dx.doi.org/10.1016/j.jmps.2018.11.020.

Gorissen, B., Melancon, D., Vasios, N., Torbati, M., Bertoldi, K., 2020. Inflatable soft jumper inspired by shell snapping. Science Robotics 5 (42), 1967. http://dx.doi.org/10.1126/scirobotics.abb1967.

Gorissen, B., Reynaerts, D., Konishi, S., Yoshida, K., Kim, J.W., De Volder, M., 2017. Elastic inflatable actuators for soft robotic applications. Adv. Mater. 29 (43), 1–14. http://dx.doi.org/10.1002/adma.201604977.

Hoang, S., Karydis, K., Brisk, P., Grover, W.H., 2021. A pneumatic random-access memory for controlling soft robots. PLoS One 16 (7 July), 1–25. http://dx.doi.org/10.1371/journal.pone.0254524.

Hubbard, J.D., Acevedo, R., Edwards, K.M., Alsharhan, A.T., Wen, Z., Landry, J., Wang, K., Schaffer, S., Sochol, R.D., 2021. Fully 3D-printed soft robots with integrated fluidic circuitry. Sci. Adv. 7 (29), http://dx.doi.org/10.1126/sciadv.abe5257.

Ilievski, F., Mazzeo, A.D., Shepherd, R.F., Chen, X., Whitesides, G.M., 2011. Soft robotics for chemists. Angew. Chemie - Int. Ed. 50 (8), 1890–1895. http://dx.doi.org/10.1002/anie.201006464.

Jin, L., Yang, Y., Maldonado, B.O.T., Lee, S.D., Figueroa, N., Full, R.J., Yang, S., 2023. Ultrafast, programmable, and electronics-free soft robots enabled by snapping metacaps. Adv. Intell. Syst. 5 (6), 2300039. http://dx.doi.org/10.1002/aisy.202300039.

Khalil, H., 2002. Nonlinear Systems. In: Pearson Education, Prentice Hall.

Laschi, C., Mazzolai, B., Cianchetti, M., 2016. Soft robotics: Technologies and systems pushing the boundaries of robot abilities. Science Robotics 1 (1), 1–12. http://dx.doi.org/10.1126/scirobotics.aah3690.

Lee, A., Jiménez, F.L., Marthelot, J., Hutchinson, J.W., Reis, P.M., 2016. The geometric role of precisely engineered imperfections on the critical buckling load of spherical elastic shells. J. Appl. Mech. Trans. ASME 83 (11), 1–11. http://dx.doi.org/10.1115/1.4034431.

Liu, T., Chen, Y., Hutchinson, J.W., Jin, L., 2022. Buckling of viscoelastic spherical shells. J. Mech. Phys. Solids 169 (October), 105084. http://dx.doi.org/10.1016/j.jmps.2022.105084.

Mahon, S.T., Buchoux, A., Sayed, M.E., Teng, L., Stokes, A.A., 2019. Soft robots for extreme environments: Removing electronic control. In: RoboSoft 2019 - 2019 IEEE Int. Conf. Soft Robot.. pp. 782–787. http://dx.doi.org/10.1109/ROBOSOFT.2019.8722755.

Marthelot, J., Jiménez, F.L., Lee, A., Hutchinson, J.W., Reis, P.M., 2017. Buckling of a pressurized hemispherical shell subjected to a probing force. J. Appl. Mech. Trans. ASME 84 (12), http://dx.doi.org/10.1115/1.4038063.

McDonald, K., Ranzani, T., 2021. Hardware methods for onboard control of fluidically actuated soft robots. Front. Robot. AI 8 (August), 1–19. http://dx.doi.org/10.3389/frobt.2021.720702.

Napp, N., Araki, B., Tolley, M.T., Nagpal, R., Wood, R.J., 2014. Simple passive valves for addressable pneumatic actuation. In: 2014 IEEE Int. Conf. Robot. Autom.. IEEE, pp. 1440–1445. http://dx.doi.org/10.1109/ICRA.2014.6907041.

Overvelde, J.T.B., Kloek, T., D'haen, J.J.A., Bertoldi, K., 2015. Amplifying the response of soft actuators by harnessing snap-through instabilities. Proc. Natl. Acad. Sci. 112 (35), 10863–10868. http://dx.doi.org/10.1073/pnas.1504947112.

Pandey, A., Moulton, D.E., Vella, D., Holmes, D.P., 2014. Dynamics of snapping beams and jumping poppers. EPL (Europhys. Lett. 105 (2), 24001. http://dx.doi.org/10.1209/0295-5075/105/24001.

Park, T., Choi, E., Kim, C.S., Park, J.O., Hong, A., 2022. A multi-segmented soft finger using snap-through instability of a soft valve with a slit. IEEE Robot. Autom. Lett. 7 (3), 6990–6997. http://dx.doi.org/10.1109/LRA.2022.3180037.

Reis, P.M., 2015. A perspective on the revival of structural (in) stability with novel opportunities for function: From buckliphobia to buckliphilia. J. Appl. Mech. Trans. ASME 82 (11), 111001. http://dx.doi.org/10.1115/1.4031456.

Rich, S.I., Wood, R.J., Majidi, C., 2018. Untethered soft robotics. Nat. Electron. 1 (2), 102–112. http://dx.doi.org/10.1038/s41928-018-0024-1.

Rothemund, P., Ainla, A., Belding, L., Preston, D.J., Kurihara, S., Suo, Z., Whitesides, G.M., 2018. A soft, bistable valve for autonomous control of soft actuators. Science Robotics 3 (16), eaar7986. http://dx.doi.org/10.1126/scirobotics.aar7986.

Rus, D., Tolley, M.T., 2015. Design, fabrication and control of soft robots. Nature 521 (7553), 467–475. http://dx.doi.org/10.1038/nature14543.

Song, S., Joshi, S., Paik, J., 2021. CMOS-inspired complementary fluidic circuits for soft robots. Adv. Sci. 2100924. http://dx.doi.org/10.1002/advs.202100924.

Taffetani, M., Jiang, X., Holmes, D.P., Vella, D., 2018. Static bistability of spherical Caps. Proc. R. Soc. A Math. Phys. Eng. Sci. 474 (2213), http://dx.doi.org/10.1098/rspa.2017.0910.

Teichmann, J., Auth, P., Conrad, S., Speck, T., Tauber, F.J., 2023. An insect-inspired soft robot controlled by soft valves. In: Meder, F., Hunt, A., Margheri, L., Mura, A., Mazzolai, B. (Eds.), Biomimetic and Biohybrid Systems. Springer Nature Switzerland, Cham, pp. 428–441.

Van Laake, L.C., De Vries, J., Kani, S.M., Overvelde, J.T.B., 2022. A fluidic relaxation oscillator for sequential actuation in soft robots. Matter 1–20. http://dx.doi.org/10.1016/j.matt.2022.06.002.

Van Raemdonck, B., Milana, E., De Volder, M., Reynaerts, D., Gorissen, B., 2023. Nonlinear inflatable actuators for distributed control in soft robots. Adv. Mater. 35 (35), 2301487. http://dx.doi.org/10.1002/adma.202301487.

Vasios, N., Gross, A.J., Soifer, S., Overvelde, J.T., Bertoldi, K., 2020. Harnessing viscous flow to simplify the actuation of fluidic soft robots. Soft Robot. 7 (1), 1–9. http://dx.doi.org/10.1089/soro.2018.0149.

Wehner, M., Truby, R.L., Fitzgerald, D.J., Mosadegh, B., Whitesides, G.M., Lewis, J.A., Wood, R.J., 2016. An integrated design and fabrication strategy for entirely soft, autonomous robots. Nature 536 (7617), 451–455. http://dx.doi.org/10.1038/nature19100.

Welty, J., Wicks, C., Wilson, R., Rorrer, G., 2007. Fundamentals of Momentum, Heant, and Mass Transfer.

Zhai, Y., Boer, A.D., Yan, J., Shih, B., Faber, M., Speros, J., Gupta, R., Tolley, M.T., 2023. Desktop fabrication of monolithic soft robotic devices with embedded fluidic control circuits. Science Robotics 8 (79), eadg3792. http://dx.doi.org/10.1126/scirobotics.adg3792.